Journal of Petroleum Science and Engineering 214 (2022) 110499

Contents lists available at ScienceDirect

Journal of Petroleum Science and Engineering

journal homepage: www.elsevier.com/locate/petrol

Occurrence characteristics of the movable fluid in heterogeneous sandstone reservoir based on fractal analysis of NMR data: A case study of the Chang 7 Member of Ansai Block, Ordos Basin, China

Qibiao Zang [a,b], Chenglin Liu [a,b,*], Rizwan Sarwar Awan [a,b,**], Xiya Yang [a,b], Guoxiong Li [a,b], Yuping Wu [a,b], Zhendong Lu [a,b], Dehao Feng [a,b]

[a] College of Geosciences, China University of Petroleum, Beijing, 102249, China
[b] State Key Laboratory of Petroleum Resource and Prospecting, China University of Petroleum, Beijing, 102249, China

ARTICLE INFO

Keywords:
Tight sandstone reservoir
Fractal dimension
Movable fluid saturation
Nuclear magnetic resonance
Pore structure

ABSTRACT

In the Ordos Basin, Chang 7 sandstone is considered an essential tight sandstone reservoir. In this research, the occurrence characteristics of the movable fluid, fractal characteristics, and their relationship in Chang 7 reservoir of the Ansai Block, Ordos Basin, have been quantitatively evaluated through nuclear magnetic resonance (NMR) and fractal theory. Moreover, the factors influencing the fractal dimensions and movable fluid distribution have been determined through a series of experiments, i.e., conventional physical property, cast thin section, scanning electron microscope (SEM), high-pressure mercury intrusion (HPMI), and X-ray diffraction technique (XRD). It has been noticed the movable fluid distribution in the tight sandstone reservoirs is greatly affected by the pore structure heterogeneity. Results show the main pore types in Chang 7 are the intergranular dissolution pores, intragranular dissolution pores, residual intergranular pores, and inter-crystalline pores. The pore size chiefly ranges from 0.1 nm–5 μm, while the main fluids storage spaces are nanopores and submicron pores. The reservoir has been divided into three types (type I, II, and III) based on the distribution of the T_2 spectrum and petrophysical parameters. Moreover, these reservoirs have various movable fluid distributions and fractal structures. Multiple factors such as pore structure, pore size distribution, and mineral compositions are discussed, which influence the fractal dimension and movable fluid saturation. The reservoirs having more nanopores are often associated with strong heterogeneity and low movable fluid content. The fractal dimension is weakly affected by pore structure parameters and mineral compositions. The movable fluid saturation is significantly affected by pore structure while weakly affected by mineral compositions. The relationship between heterogeneity and movable fluid distribution varies with reservoir types. The inhibition of heterogeneity on the movable fluid of different reservoirs is mainly reflected in various pores. Movable fluids controlled by throats are primarily distributed in different pores, resulting in diverse effects of heterogeneity on controlling the effect of different throats in various reservoirs. The findings of this research can help better understand the occurrence characteristics of the movable fluid in tight sandstone reservoirs with different fractal features.

Credit author statement

Qibiao Zang and Chenglin Liu conceived of the presented idea. Xiya Yang, Guoxiong Li, Zhendong Lu and Dehao Feng have collected the data and carried out the experiments. Qibiao Zang wrote the manuscript with support from Rizwan Sarwar, Chenglin Liu, and Yuping Wu. All authors discussed the results and contributed to the final manuscript.

1. Introduction

In the last few decades, conventional oil and gas resources have been declining, and global oil and gas resources have faced huge challenges (Awan et al., 2021; Tong et al., 2018). Experts and scholars have paid great attention to the exploration and development of tight oil resources. Tight sandstone reservoirs in China are defined as reservoirs with an in situ permeability of less than 0.1×10^{-3} μm^2 (or air permeability of less

* Corresponding author. College of Geosciences, China University of Petroleum, Beijing, 102249, China.
** Corresponding author. College of Geosciences, China University of Petroleum, Beijing, 102249, China.
E-mail addresses: lclzgx@126.com (C. Liu), rsageoche@gmail.com (R.S. Awan).

https://doi.org/10.1016/j.petrol.2022.110499
Received 10 May 2021; Received in revised form 1 February 2022; Accepted 7 April 2022
Available online 11 April 2022

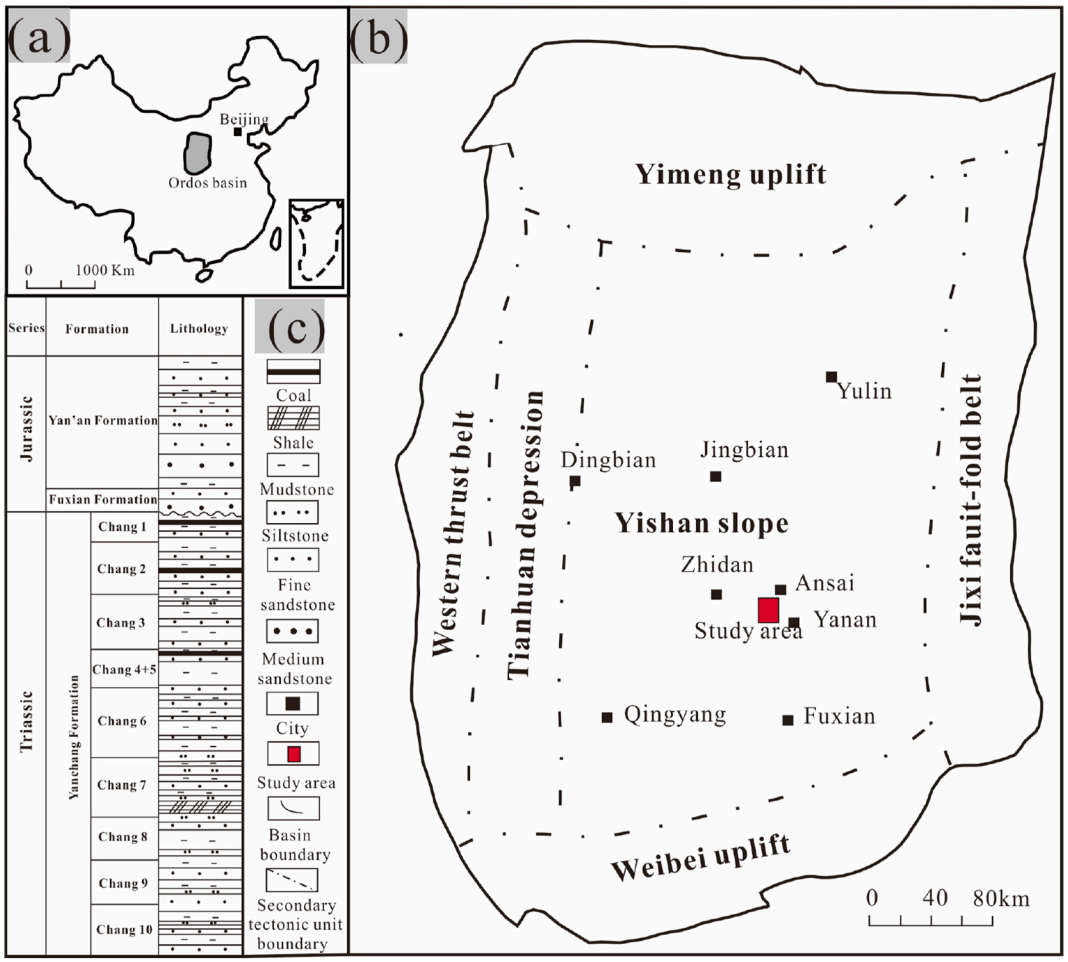

Fig. 1. Location and stratigraphic units of the study area: (a). Location of Ordos Basin in China; (b). Regional overview of the Ordos Basin and the location of the study area; (c). Stratigraphic division and lithological characteristics in the study area.

than 1.0×10^{-3} μm^2) and porosity of <10% (Zou et al., 2012). Tight sandstone reservoirs are characterized by low porosity and permeability, the complexity of pore structure and oiliness, strong heterogeneity, and low petroleum recovery (Clarkson et al., 2012a; Jia et al., 2012; Rezaee et al., 2012; Zou et al., 2012). Therefore, the exploration and development of tight sandstone oil resources are challenging. The pore structure characteristics are the key factors causing the great difference between the movable fluid distribution in tight sandstone reservoirs and conventional reservoirs (Clarkson et al., 2012b; Dai et al., 2019). The pore structures of tight sandstone reservoirs are usually characterized by various degrees of connectivity and heterogeneity (Cao et al., 2016; Desbois et al., 2011; Zhou et al., 2019). Chang 7 member has great oil and gas exploration potential and is considered as an unconventional oil and gas production base in Ordos Basin (Yang et al., 2016). Scholars have carried out massive research on the micro pore structure characteristics of Chang 7 sandstone through various technologies (Guo et al., 2020; Lai et al., 2016; Qin et al., 2021; Wang et al., 2020b; Yan et al., 2020; Yuan et al., 2015). It has been noticed the storage space of Chang 7 sandstone is mainly due to micro-nano-scale pores (Guo et al., 2020; Li et al., 2019a; Yan et al., 2020; Yuan et al., 2015). The characteristics of small pore throats, complex pore structure, strong heterogeneity, and poor connectivity lead to difficult fluid seepage (Li et al., 2019a; Xu et al., 2021; Yan et al., 2020). The characteristics of pore structure can be analyzed by pore size, connectivity, uniformity, and sorting through various experiments, i.e., Nuclear magnetic resonance (NMR), X-ray computed tomography (CT), scanning electron microscope (SEM), and high-pressure mercury intrusion (HPMI) (Chen et al., 2018; Eslami et al., 2013; Huang et al., 2020; Lai et al., 2018b; Oluwadebi et al., 2019; Schmitt et al., 2016; Shabaninejad et al., 2018; Zhang et al., 2019). The fractal theory has been widely used to analyze the irregularity and complexity of pore structure in porous media since Mandelbrot proposed the fractal concept (Mandelbrot et al., 1984). NMR, HPMI, and N_2 adsorption are often used to analyze the fractal characteristics of sandstone, shale, carbonate, and coal (Amadu and Pegg, 2018; Li et al., 2019b; Schmitt Rahner et al., 2018; Wu et al., 2021; Zang et al., 2021b). Fractal dimension is an important parameter to characterize the heterogeneity of pore structures, which has a considerable impact on fluid distribution and flow capabilities in tight sandstone reservoirs (Zhang et al., 2021; Zhang and Andreas, 2014). The fractal dimension of porous rock ranges from 2 to 3, reflecting pore structure characteristics (Amadu and Pegg, 2018; Li et al., 2019b; Wu et al., 2021; Zhao et al., 2017). The large fractal dimension often corresponds to more small pores, rough pore surface, poor interconnectivity, and strong heterogeneity.

Fluids in the pores of tight sandstone reservoirs can be divided into movable fluids and bound fluids. The free state fluids in the connected pores are called movable fluids (Timur, 1969). Due to capillary forces and viscous forces, the fluids in tiny pores are in the bound state known as bound fluids (Gao and Li, 2015; Li et al., 2018b; Mozley et al., 2016). The recovery of tight sandstone oil is affected by the content and distribution of movable fluid in pores. The movable fluid saturation (S_m) is a significant parameter to evaluate the movable fluid content, reflecting movable fluid's occurrence characteristics in pores (Gao and Li, 2015; Mao et al., 2020). NMR test and centrifugal experiments are direct and

quick techniques to assess movable fluid saturation. The movable fluids are the only valuable resource in the tight sandstone reservoir. Therefore, conducting an in-depth analysis of fluid fluidity in a tight sandstone reservoir is significant. NMR has been widely used in various fields of geosciences because of its advantages of rapidity, non-destructive, and repeatability (Chen et al., 2018; Rosenbrand et al., 2015; Testamanti and Rezaee, 2017; Zhou et al., 2019). NMR can be used to analyze the fractal dimension and fluids occurrence characteristics in pores and other geological information related to pore structure and physical properties by detecting the proton (1H) NMR signal of the water's hydrogen in the pore (Fan et al., 2019; Hossain et al., 2011; Mao et al., 2005; Zhao et al., 2017). NMR T_2 relaxation time (T_2) is related to the pore size. Some researcher has proposed different methods for transforming T_2 spectra into pore size based on HPMI (Dai et al., 2019; Huang et al., 2020; Yao and Liu, 2012). Therefore, combined with centrifugal experiments, NMR can distinguish the movable fluids from the irreducible fluids and analyze the movable fluids distribution in different pores.

The distribution of pore size, pore interconnectivity, and heterogeneity of the pore structures is closely related to movable fluids' occurrence characteristics. Previous studies mainly focused on the evaluation of relevant movable fluid parameters, different pore types, and the correlation between pore structures and physical properties (Gao and Li, 2015; Li et al., 2019a; Mao et al., 2020; Testamanti and Rezaee, 2017; Wang et al., 2020a, 2020b). However, little attention has been paid to the occurrence characteristics and influencing factors of movable fluid. Moreover, the influence of heterogeneity on the occurrence characteristics of the movable fluid in different pores is ignored. Therefore, this research better characterizes the occurrence characteristics of the movable fluid in tight sandstone reservoirs with different fractal structures. It also elaborates on the occurrence characteristics of the movable fluid and the fractal characteristics and their relationship in tight sandstone using NMR technology. Moreover, cast thin sections (CTS), SEM, HPMI, and XRD, are also carried out to quantitatively analyze fractal characteristics and movable fluid distribution factors, providing a theoretical basis for enhancing the recovery of tight sandstone oil.

2. Geological setting

The Ordos Basin is a superimposed craton depression basin considered an essential petroliferous basin in China. It has been divided into six first-order tectonic units, including the Yimeng uplift, Weibei uplift, Jinxi flexure belt, Yishan slope, Tianhuan depression, and West Rim thrust belt (Liu and Yang, 2000; Yang et al., 2005) (Fig. 1). A total of 19 sandstone samples were drilled from Chang 7 of the Upper Triassic Yanchang Formation in the Ansai Block, which is located in the tectonic unit of the Yishan Slope in the Midsouth Ordos Basin. The Chang 7 Member in the study area inherits the overall characteristics of the Yishan slope, where the structures are gentle. The Chang 7 Member in the Ansai area is a typical delta front sedimentary system (Cui et al., 2019; Fu et al., 2018). It developed various sedimentary microfacies, i.e., underwater distributary channels, mouth bars, and sheet sands (Cui et al., 2019; Fu et al., 2018; Zhang et al., 2020b). Chang 7 Member contains plenty of oil and gas resources because the sandstone reservoir has a conformable contact with the source rock. The characteristics of these sandstone reservoirs are as follows: (1) fine grain size, (2) high argillaceous content, (3) a complex mineral composition, (4) poor petrophysical properties.

3. Methods and samples

3.1. Physical properties and XRD

The porosity, permeability, and mineral composition of a reservoir are essential in evaluating the reservoir quality (Qiao et al., 2020b). Prior to the relevant pore structure tests, the samples need to be tested for porosity and permeability using JS 100007 helium porosimeter and A-1013 gas permeameter. X-ray diffraction can analyze the quantitative amount of various mineral compositions in a rock sample. The mineral composition determines the crystal structure affecting the diffraction intensity (Elton and Salt, 1996). Equation (Eq.) 1 reveals the relationship between the spatial orientation of diffraction lines and crystal structure (Pope, 1997).

$$n\lambda = 2d\sin\theta \tag{1}$$

where: θ, λ, and d are the incident angle, wavelength, and interplanar spacing, respectively.

3.2. HPMI

HPMI can be used to characterize the pore structure of tight sandstone by injecting mercury into the rock under different pressures. An AutoPore IV 9505 mercury porosimeter produced by Quantachrome of the United States is used in this research. The applied pressure is between 3.5 kPa and 119.7 MPa, and the corresponding pore-throat radius is between 210.2 μm and 6.1 nm. Under external pressure, mercury enters the pore system of the rock sample by overcoming capillary resistance. Different pressures correspond to different pore sizes. The capillary pressure curve can be obtained by recording the amount of mercury under different pressures. The shape of the capillary pressure curve is affected by pore size and distribution. Besides, according to the results of HPMI, a series of relevant parameters, such as displacement pressure, median pressure, maximum pore radius, median pore radius, skewness, sorting coefficient, maximum mercury saturation, and minimum mercury residual saturation, can be obtained thoroughly to characterize the pore structure of tight sandstone reservoir (Daigle and Johnson, 2015; Yao and Liu, 2012; Zhang et al., 2019). The relationship between capillary pressure and pore throat radius is as follows (Washburn, 1921):

$$P_c = -\frac{2\sigma\ cos\ \theta}{r} \tag{2}$$

where: P_c is the capillary force, MPa, σ is the interfacial tension, mN/m, θ is the contact angle, and r is the pore radius, μm.

3.3. NMR and centrifugation

NMR is an effective technique to analyze the occurrence characteristics of the movable fluid in tight sandstone reservoirs. The transverse relaxation time T_2 can quantitatively characterize fluid distribution in different pores based on the inverse relation between pore size and hydrogen nuclear relaxation rate (Al-Mahrooqi et al., 2006; Chen et al., 2018; Eslami et al., 2013; Liu et al., 2020). Due to the difference in petrophysical properties and fluid properties, the shape of the T_2 spectrum varies with the pore structures of tight sandstone reservoirs.

NMR test was carried out on 19 samples at the State Key Laboratory of Petroleum Resources and Prospecting, China University of Petroleum (Beijing). Maran-drx/2 NMR instrument equipped with two pulsed gradient magnetic fields is used for core NMR measurement. It can be used for rapid testing with high accuracy. The main working parameters of the instrument are as follows: the test temperature is 35 °C, the number of echoes is 8192, the working frequency is 2 MHz, the echo interval is 0.1 ms, and the gain is 80%. The preliminary steps were as follows: 1) The samples were washed and measured for porosity and permeability. 2) The samples were placed in the oven for 72 h at 85 °C, then the dried specimens were weighed and measured, and the mass, diameter, and length of samples were recorded. 3) After that, samples were saturated in simulated formation water (1.8% NaCl solution) with a saturation pressure of 15 MPa for 36 h. The weight of the sample in the water-saturated state was measured again. 4) NMR experiments measured the T_2 spectrum distribution of 100% water-saturated cores. Then the samples are centrifuged under centrifugal forces of 42 psi, 208

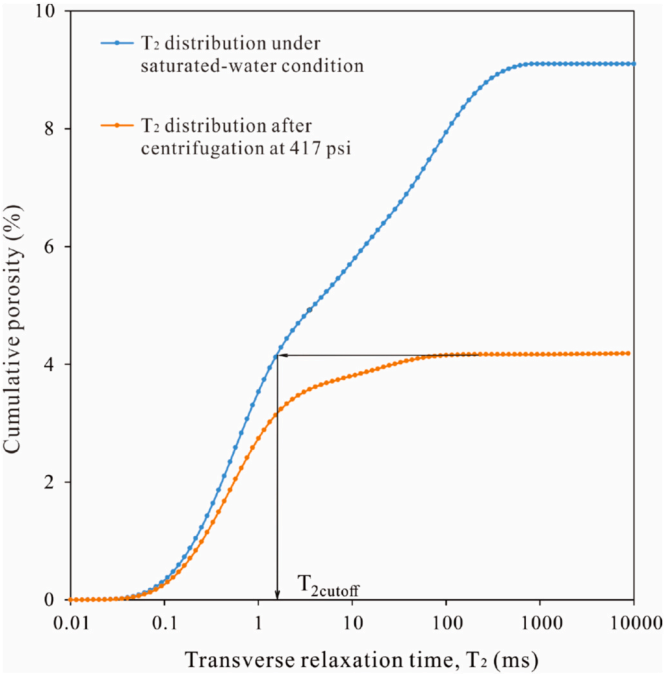

Fig. 2. Illustration of the method to calculate the T_2 cutoff value.

Table 1
Petrophysical properties of samples from Chang 7 sandstone reservoir.

No	Well	Depth (m)	Lithology	$T_{2cutoff}$ (ms)	Porosity (%)	Permeability ($\times 10^{-3}\mu m^2$)
1	D201	1666.88	Siltstone	1.60	8.68	0.0470
2	G62	1606.28	Siltstone	39.10	9.75	0.1148
3	Q168	1664 .00	Siltstone	4.34	9.22	0.0200
4	Q195	1054.13	Siltstone	7.48	9.29	0.0860
5	D201	1227.75	Siltstone	5.02	12.18	0.1617
6	Q129	1669.16	Siltstone	1.50	5.73	0.0250
7	Q71	1436.2	Siltstone	1.16	4.5	0.0100
8	Z22-31	1248.26	Siltstone	4.93	5.97	0.0110
9	G62	1603.15	Siltstone	3.72	7.23	0.0199
10	Q71	1428.45	Argillaceous siltstone	2.01	3.90	0.0072
11	D199	1372.83	Argillaceous siltstone	1.91	6.60	0.0280
12	Q71	1437.2	Siltstone	2.35	4.78	0.0190
13	G62	1607.06	Siltstone	2.70	5.02	0.0031
14	Q71	1434.54	Argillaceous siltstone	2.80	5.97	0.0026
15	Q71	1434.9	Siltstone	1.65	5.70	0.0101
16	Q71	1427.26	Argillaceous siltstone	11.32	5.20	0.0086
17	Q71	1429.82	Argillaceous siltstone	28.48	4.25	0.0019
18	Q71	1426.2	Siltstone	2.55	6.62	0.0042
19	Q203	1451.6	Siltstone	12.21	4.453	0.0051

psi, and 417 psi (100 psi = 0.689 MPa) for 1.5 h. The samples' mass and T_2 spectral distribution are measured after each centrifugation. The water left in the samples after centrifugation at 417 psi is considered irreducible water.

Centrifugation is the centrifugal force generated by a high-speed centrifuge to force the wetting phase to replace the non-wetting phase in the core. The phases in this experiment are gas and water. Under high-speed centrifugation, water is eliminated from the pores, and centrifugal force is balanced with capillary force. The relationship between centrifugal force and rotational speed is as follows (Deng et al., 2014; Machabeli and Rogava, 1994):

$$G = 1.188 * 10^{-5} * N^2 * R \quad (3)$$

where: G is the centrifugal force. It is usually represented by a multiple of the gravitational acceleration g (9.8 m/s^2). N is rotational speed, r/min; R is the centrifugal radius, cm.

3.4. CTS and SEM

CTS can obtain information about the pore and throat morphology, surface porosity, pore-throat coordination number, debris composition, etc. CTS can be prepared by injecting the infusion fluids matched with oil-soluble dyes (red, blue) epoxy resin into the pores. The production process of CTSs follows the rock-thin section preparation (SY/T 5913–2004). The final sample is polished with a thickness of 0.03 mm. SEM analysis is carried out on the gold-coated thin sections using FEI Quanta 200 F SEM to analyze the characteristics of pore distribution, pore and throat morphology, clay minerals occurrence patterns, and other related information. The acceleration voltage of the instrument is between 200 V and 30 KV, the resolution is 1.2 nm, and the magnification is between 25 and 200,000.

3.5. T_2 cutoff and pore size reconstruction based on NMR data

The T_2 cutoff value is critical for analyzing movable fluid in the NMR test. Several factors, i.e., lithology, fluid properties, pore structure, etc., have an impact on T_2 cutoff (Ge et al., 2015; Testamanti and Rezaee, 2017; Zang et al., 2021a; Zhao et al., 2021). As shown in Fig. 2, the T_2 spectrum cumulative curve of the water-saturated core and after centrifugation at 417psi can be used to determine the T_2 cutoff. Firstly, a horizontal projection from the cumulative curve after centrifugation at 417 psi is drawn (Gao and Li, 2015; Li et al., 2019a; Wang and Zeng, 2020). Then, the T_2 cutoff value can be determined through the intersection of this projection line and the cumulative T_2 spectrum under water-saturated conditions. The T_2 cutoff values of samples are shown in Table 1. The T_2 cutoff values of Chang 7 tight sandstone are located between 1.2 ms and 39.1 ms (the majority is distributed mainly between 1.50 ms and 8.00 ms).

A non-destructive NMR test can accurately measure the distribution characteristics of pore size. The transverse relaxation time T_2 is closely related to the pore size. The bulk transversal relaxation time is far greater than the transverse relaxation time. Therefore, the bulk relaxation time can usually be ignored. Additionally, in the NMR experiment, the diffusion relaxation time can be ignored when the magnetic field is uniform (Lai et al., 2019; Li et al., 2018a; Timur, 1969). Therefore, the transverse relaxation time T2 can be expressed by the following formula (Jorand et al., 2011; Tinni et al., 2015; Wu et al., 2019):

$$\frac{1}{T_2} = \rho \frac{S}{V} \quad (4)$$

Meanwhile,

$$\frac{S}{V} = \frac{Fs}{r} \quad (5)$$

where: T_2 is the transverse relaxation time (ms), and ρ is the surface relaxation rate (μm/ms). Fs is the shape factor (Fs = 2 or 3 is for cylindrical or spherical pores), r is the pore-throat radius (μm), and S/V is the porous specific area.

The relationship between transverse relaxation time (T_2) and pore-throat radius (r) can be expressed via Eq. (6).

$$1 / T_2 = Fs * \rho / r \quad (6)$$

when C= Fs*ρ, Eq. (6) can be transformed into Eq. (7).

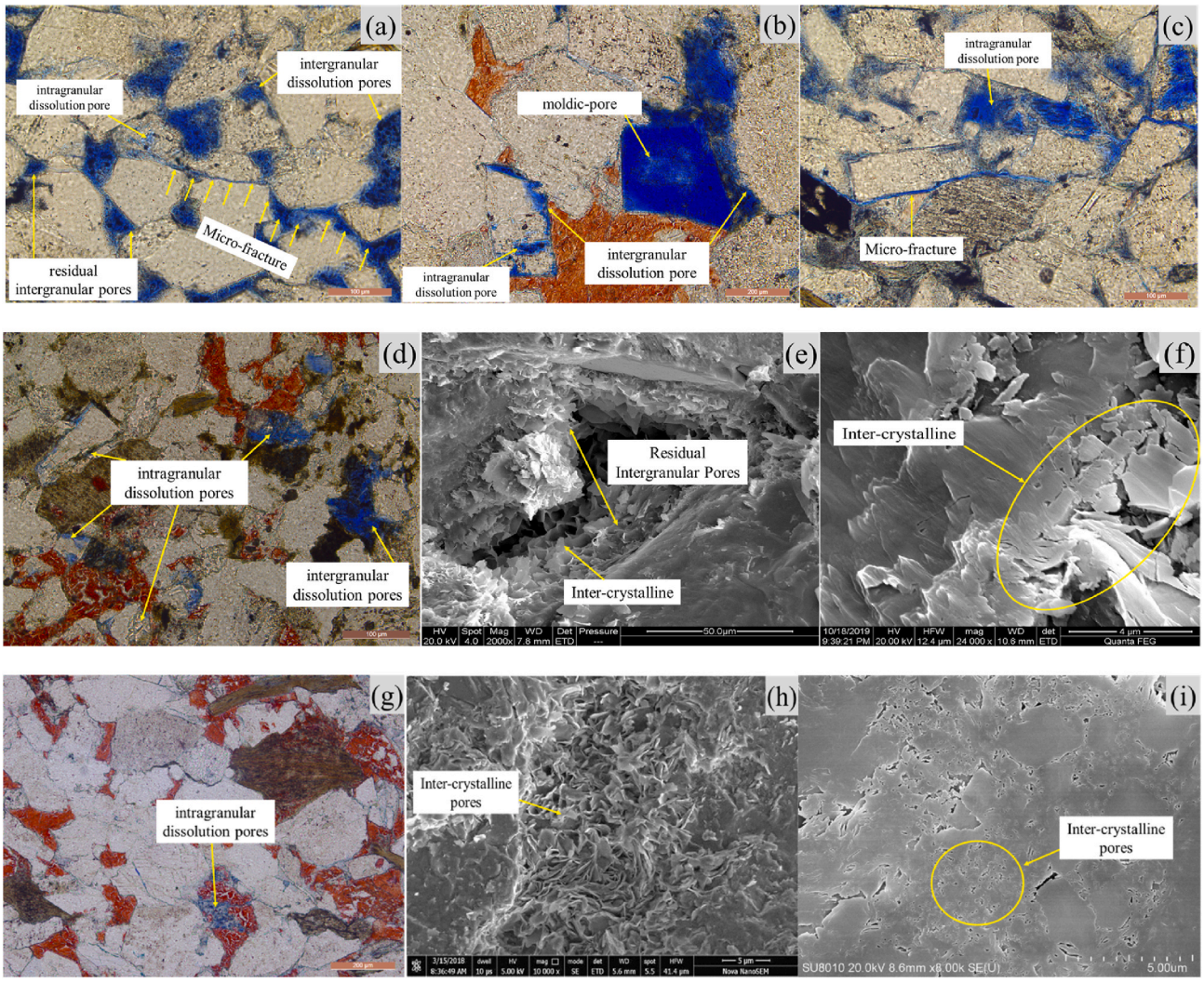

Fig. 3. Pore types of Chang 7 tight sandstone.(a)-#1: residual intergranular pores, intergranular dissolution pores, intragranular dissolution pores and micro-fracture (CTS); (b)-#2: intergranular dissolution pores, intragranular dissolution pores and moldic pore (CTS); (c)-#3: intragranular dissolution pores and micro-fracture (CTS); (d)-#8: intergranular dissolution pores and intragranular dissolution pores (CTS); (e)-#10: inter-crystalline pores and residual intergranular pores (SEM); (f)-#6: inter-crystalline pores (polished sample) (SEM); (g)-#15: intragranular dissolution pores (CTS); (h)-#15: inter-crystalline pores (SEM); (i)-#16: inter-crystalline pores (polished sample) (SEM).

$$d = CT_2 \tag{7}$$

where: d is the pore-throat diameter (μm). Previous studies have proposed many methods for transforming T_2 spectra into pore size distribution based on HPMI (Chen et al., 2018; Yao and Liu, 2012). However, those methods are practically not convenient due to uncertain estimation errors. Therefore, the most convenient and practical method is used in this study. The pore size d (corresponding to the centrifugation at 417psi, 100 psi = 0.689 MPa) and T_2 cutoff are used in this research. Moreover, according to Eq. (2) ($\sigma = 480$ mN/m, $\theta = 140°$), d is 0.05 μm for any sample in this study. Since any relaxation time corresponds to certain pore size, Eq. (8) can be obtained.

$$C = 0.05/T_{2cutoff} \tag{8}$$

Therefore, the relationship between the transverse relaxation and pore size can be established Eq. (9). Where: d_{ci} is a pore size corresponding to a relaxation time T_{2i} (ms), (μm).

$$d_{ci} = 0.05 * T_{2i}/T_{2cutoff} \tag{9}$$

3.6. Core samples

Nineteen oil-bearing samples are collected from Chang 7 tight sandstone reservoir in the Ansai area of Ordos Basin. This research utilized the wire cutting instrument to prepare the required parallel cylindrical sample to ensure no artificial fractures in the parallel columnar samples. The diameter of the molybdenum wire used in the wire cutting instrument was 0.13 mm, which provides the flatness of samples. No obvious external force is applied to the cylindrical sample in the sample preparation process, confirming no artificial fractures. The lithology of the samples includes siltstone argillaceous and siltstone. Samples are divided into several parts for a series of experiments, including porosity, permeability, NMR, HPMI, XRD, SEM, and thin casting sections, to analyze the occurrence characteristics of the movable fluid in different pores. All samples are analyzed for the NMR technique. Other supporting experiments are as follows: thin casting sections (19 samples), SEM (19 samples), porosity and permeability tests (19 samples), HPMI tests (13 samples), and XRD (12 samples).

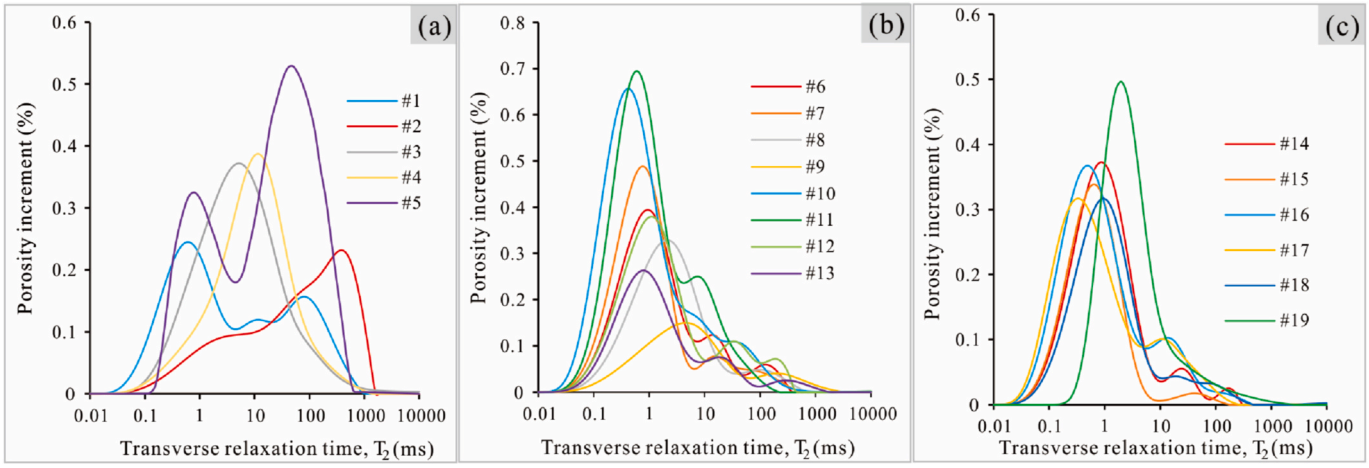

Fig. 4. NMR T_2 spectra distribution of samples. (a): Type I; (b): Type II; (c): Type III

4. Results

4.1. Petrophysical properties and pore types

4.1.1. Petrophysical properties

The porosity and permeability of samples are listed in Table 1. The porosity ranges between 3.90–12.18% (mean 6.69%). The permeability ranges from 0.0019 × 10^{-3}μm^2 to 0.1617 × 10^{-3}μm^2 (mean 0.0310 × 10^{-3}μm^2). In this research, most samples reveal the lower values of permeability (<0.1 × 10^{-3}μm^2) and lower porosity values (<10%), which suggest that the sandstone of the Chang 7 Member is a tight sandstone reservoir.

4.1.2. Pore types

According to microscopic observation, the pore types of Chang 7 sandstone samples in Ansai Block can be divided into five categories: i. Intergranular dissolution pores, ii. Intragranular dissolution pores, iii. Residual intergranular pores, iv. Inter-crystalline pores, v. Micro-fractures (Fig. 3). Intergranular dissolution pores are formed by the dissolution of the mineral particles (such as feldspar) or cement (such as carbonates). Intergranular dissolution pores with better connectivity often appear as irregular edges and mostly in the shape of a harbor. The longer dimensions of these pores range between 2.00 μm and 100.00 μm (Fig. 3a, b, d). Intragranular dissolution pores are mainly distributed in feldspar grains and often develop along cleavage (Fig. 3a–d). The connectivity of these pores is relatively poor and often has an irregular geometry. The size of these pores is chiefly in the range of 0.50–50.00 μm. Additionally, a small number of moldic-pores can be seen in some samples (Fig. 3b). The mechanical compaction and cementation usually alter residual intergranular pores. Most pores are regular triangles or polygons, distinguished from intergranular dissolution pores. Residual intergranular pores usually appear in the combinational form, e.g., dissolution - residual intergranular pores and inter-crystalline - residual intergranular pores (Fig. 3a and e). There are many inter-crystalline pores in the tight sandstone in the study area (Fig. 3e, f, h, i). Such pores often appear on the walls of dissolution pores and residual intergranular pores or the surface of particles. The size of inter-crystalline pores is between 0.02–1.00 μm. A few micro-fractures are available in the study area with good connectivity (Fig. 3a, c). These micro-fractures are related to sedimentation, diagenesis, and tectonic stress. It greatly promotes fluid migration in tight reservoirs. Additionally, it can be seen from CTS that some samples (such as samples #1 and #4) have the characteristics of high porosity and permeability, which may be related to the development of more intergranular dissolution pores and a few micro-fractures and moldic-pores (Fig. 3a and b).

4.2. T_2 spectra distribution and pore size distribution obtained from NMR data

4.2.1. T_2 spectra distribution

The T_2 spectra of samples under saturated-water conditions are shown in Fig. 4. The distribution range of T_2 spectra of Chang 7 sandstone is broad, mainly ranging from 0.05 ms to 400 ms. A small number of T_2 relaxation values greater than 1000 ms appear in sample #2, which may be related to the development of micro-fractures and oversized dissolution pores (such as moldic-pores). The T_2 spectra of the specimens under saturated-water conditions are characterized by the coexistence of unimodal peaks, bimodal peaks, and trimodal peaks. Peak position and valley vary with samples, indicating that the pore structure of tight sandstone samples in the study area is quite different. The morphological characteristics of the T_2 spectrum are closely related to the pore throat structure (Li et al., 2018a, 2019a). Eq. (7) reveals the size of $T_{2cutoff}$ constructed from NMR data is an important parameter affecting the pore size distribution. Additionally, porosity and permeability are key parameters reflecting storage and penetration capacity. Therefore, according to the distribution characteristics of the T_2 spectrum and petrophysical parameters (Table 1), the Chang 7 sandstone samples can be divided into three types: type I, II, and III. Type I is comprised of a similar number of short relaxation time (<10 ms) and long relaxation time (>10 ms) (Fig. 4a) and usually correspond to good physical properties (porosity >8%; permeability >0.03 × 10^{-3}μm^2). Similarly, type II contains a significant short relaxation time and a small number of long relaxation times (Fig. 4b). Type II are usually associated with smaller $T_{2cutoff}$ and poor physical properties (porosity <8%; 0.03 × 10^{-3}μm^2 < permeability <0.01 × 10^{-3}μm^2). In contrast, type III encompasses a significant number of short relaxation time along with few or nearly no long relaxation time (Fig. 4c), usually corresponding to larger $T_{2cutoff}$ or/and poor physical properties (porosity <8%; permeability <0.01 × 10^{-3}μm^2). The NMR T_2 spectra can reflect the pore size distribution characteristics (Chen et al., 2018). The long relaxation time is related to the larger pore, while the short relaxation time is related to the smaller pore (Xu et al., 2019; Yao and Liu, 2012). Three types of samples correspond to three types of reservoirs: type I reservoir with a similar number of small and large pores, type II reservoir with more small pores and fewer large pores, and type III reservoir with more small pores along with much few or almost no large pores. Besides, the T_2 spectrum distribution characteristics can also qualitatively reflect the pore characteristics. The reservoir with trimodal peaks means that there are various pore types, while the reservoir with unimodal peaks means that there are simple pore types.

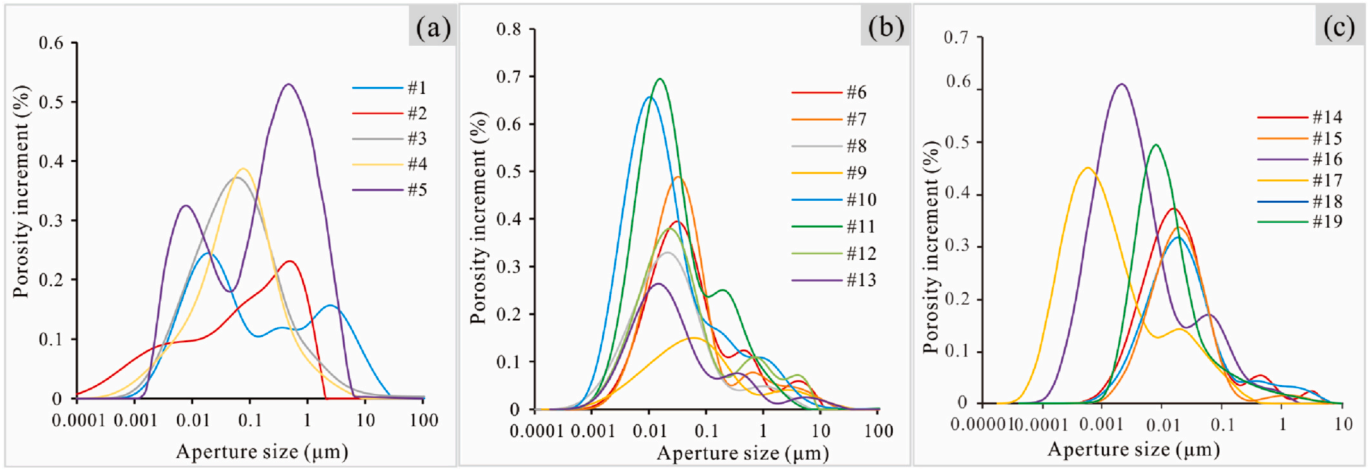

Fig. 5. Pore size distribution reconstructed from NMR data of representative samples. (a) Samples of type I reservoir; (b): Samples of type II reservoir; (c): Samples of type III reservoir.

Table 2
Petrophysical properties of Chang 7 sandstone samples based on NMR.

Reservoir Type	Sample No	Physical parameters from the NMR test					
		Nanopores		Submicron pores		Micron pores	
		Porosity, Φ_1 (%)	Proportion (%)	Porosity, Φ_2 (%)	Proportion (%)	Porosity (%)	Proportion, Φ_3 (%)
I	1	4.81	52.86	1.82	20.00	2.47	27.14
	2	4.15	52.53	3.26	41.27	0.49	6.20
	3	7.07	63.01	3.39	30.21	0.76	6.77
	4	6.27	62.64	3.30	32.97	0.44	4.40
	5	6.59	37.29	7.44	42.11	3.64	20.60
II	6	6.97	70.62	2.13	21.58	0.77	7.80
	7	8.32	79.24	1.36	12.95	0.82	7.81
	8	7.14	83.80	0.97	11.38	0.41	4.81
	9	3.01	61.43	1.22	24.90	0.67	13.67
	10	13.08	80.10	2.35	14.39	0.90	5.51
	11	12.64	77.64	3.24	19.90	0.40	2.46
	12	7.52	75.05	1.48	14.77	1.02	10.18
	13	5.25	78.59	1.02	15.27	0.41	6.14
III	14	7.37	89.12	0.71	8.59	0.19	2.30
	15	6.06	93.37	0.30	4.62	0.13	2.00
	16	14.41	93.82	0.89	5.79	0.06	0.39
	17	11.88	97.62	0.29	2.38	0.00	0.00
	18	6.11	84.98	0.76	10.57	0.32	4.45
	19	8.14	91.15	0.66	7.39	0.13	1.46

4.2.2. Pore size distribution obtained from NMR data

The T_2 spectra under saturated-water conditions can be converted to pore size distribution according to Eq. (7). Fig. 5 shows the pore size distribution constructed from NMR data of samples. The aperture size in the Chang 7 tight sandstone is mainly distributed between 1.0 nm–5.0 μm. The pore size distribution of the three types of reservoirs is quite different. The aperture size of type I reservoir mainly ranges from 2.0 nm to 5.0 μm, type II reservoir is mainly distributed between 2.0 nm and 1.0 μm, and type III reservoir is mainly distributed in the range of 1.0–200.0 nm. In some samples (e.g., sample #1), a few large pores with d > 10.0 μm may be related to the development of micro-fractures and oversized dissolution pores (such as moldic-pores). According to the pore size converted from NMR data, the pores are divided into micron pores (d > 1.0 μm), submicron pores (0.1 μm < d < 1.0 μm), and nanopores (d < 0.1 μm) to evaluate the pore size distribution characteristics. It should be noted there are only a few micro-fractures or pores with d > 10 μm are developed in some studies samples. Therefore, the micro-fractures or pores with d > 10 μm are classified as micron pores in this research.

The pore size distribution parameters are shown in Table 2. Results show the storage space of Chang 7 tight sandstone reservoir is mainly composed of nanopores, followed by submicron pores. The porosity of nanopores mainly ranges between 3.01–14.41% (mean 7.73%), accounting for 37.29–97.62% of the total pores (averaging 74.99%). The porosity of submicron pores ranges from 0.29–7.44%, with a typical value of 1.93%, accounting for 2.38–42.11% of the total pores (mean 17.95%). The pore size distribution varies with reservoir types. For type I reservoir, the storage space is mainly composed of nanopores and submicron pores. The porosity of nanopores ranges from 4.15% to 7.07% (averaging 5.78%), accounting for 37.29–63.01% (mean 53.67%). The porosity of submicron pores ranges between 1.82–7.44%, with a typical value of 3.84%, accounting for 20.00–42.11% (averaging 33.31%). A certain number of micron pores are developed in type I reservoirs. The porosity of micron pores of type I reservoir is smaller, ranging from 0.44% to 3.64% (mean 1.56%). For the type II reservoir, the storage space is mainly composed of nanopores, followed by submicron pores. The porosity of nanopores of type II mainly ranges from 3.01% to 13.08%, with a typical value of 7.99%, accounting for 61.43–83.80% of the total pores (averaging 75.81%). The porosity of submicron pores in the type II reservoir is smaller than that in the type I reservoir, ranging from 0.97% to 3.24% (mean 1.72%). There are only a few micron pores in the type II reservoirs. The porosity of nanopores of type III reservoirs ranges from 6.06% to 11.88% (mean 9.00%),

Table 3
Movable fluid distributed parameters of Chang 7 tight sandstone samples.

Reservoir Type	Sample No	S_m (%)	Movable fluid in different pores								
			Micron pores			Submicron pores			Nanopores		
			P_{p1} (%)	S_{mp1} (%)	Φ_{p1} (%)	P_{p2} (%)	S_{mp2} (%)	Φ_{p2} (%)	P_{p3} (%)	S_{mp3} (%)	Φ_{p3} (%)
I	1	54.00	46.95	25.35	2.47	27.27	14.73	1.34	26.14	14.12	1.28
	2	56.97	10.77	6.14	0.48	67.35	38.37	3.03	21.89	12.47	0.98
	3	51.68	11.42	5.90	0.66	49.76	25.72	2.88	38.82	20.06	2.25
	4	54.92	6.27	3.44	0.34	51.50	28.28	2.83	42.24	23.20	2.32
	5	65.72	25.61	16.83	2.87	65.35	42.95	7.32	9.05	5.95	1.01
II	6	42.58	16.21	6.90	0.68	40.19	17.11	1.69	39.77	16.93	1.67
	7	36.44	18.67	6.80	0.71	29.14	10.62	1.11	52.19	19.02	2.00
	8	26.78	12.53	3.36	0.29	24.96	6.68	0.57	62.51	16.74	1.42
	9	52.44	22.22	11.65	0.57	37.27	19.54	0.96	40.51	21.24	1.04
	10	25.37	12.07	3.06	0.50	20.52	5.21	0.85	67.40	17.10	2.80
	11	29.65	6.17	1.83	0.30	51.90	15.39	2.51	41.92	12.43	2.02
	12	35.43	26.07	9.24	0.93	31.79	11.26	1.13	42.18	14.94	1.50
	13	28.70	12.36	3.55	0.24	32.31	9.27	0.62	55.34	15.88	1.06
III	14	18.21	6.37	1.16	0.10	27.93	5.09	0.42	65.77	11.98	0.99
	15	16.22	3.47	0.56	0.04	6.39	1.04	0.07	90.14	14.62	0.95
	16	10.86	27.83	3.02	0.05	13.92	1.51	0.48	58.251	6.33	1.14
	17	6.23	0.00	0.00	0.00	29.37	1.83	0.20	70.63	4.40	0.56
	18	23.21	9.14	2.12	0.15	15.01	3.48	0.25	75.85	17.60	1.26
	19	12.38	8.53	1.06	0.09	17.45	2.16	0.19	74.01	9.16	0.82

Note: P_{p1}, P_{p2}, and P_{p3} are movable fluid proportions in micron pores, submicron pores, and nanopores, respectively; S_{mp1}, S_{mp2}, and S_{mp3} are movable fluid saturation in micron pores, submicron pores, and nanopores, respectively; Φ_{p1}, Φ_{p2}, and Φ_{p3} are movable fluid porosity in micron pores, submicron pores, and nanopores, respectively.

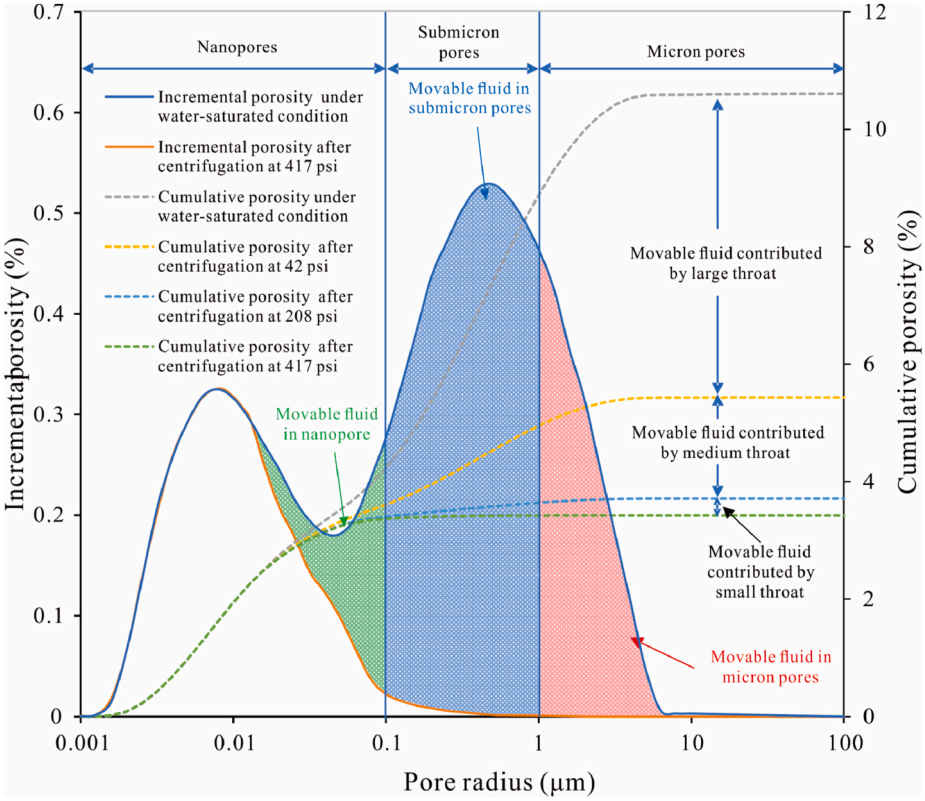

Fig. 6. Movable fluids distribution in different pores and movable fluids controlled by different throats of sample #5.

accounting for more than 80.00% of the total pores. There are very few or almost no submicron and micron pores in the type III reservoir. Different pores mainly control the storage space in these reservoirs.

4.3. Movable fluid distribution

The movable fluid saturations of the Chang 7 sandstone samples are listed in Table 3. The movable fluid saturation ranges widely and is distributed between 6.23% and 65.72% (mean 34.09%). The movable fluid saturation of tight sandstone varies with reservoir types in the study area. The movable fluid saturation of type I reservoir is the largest, ranging from 51.68% to 65.72% (averaging 56.66%), followed by type II reservoir, which is distributed between 25.37% and 52.44%, with a mean value of 34.67%. The movable fluid saturation of type III reservoir

Table 4
Movable fluid controlled by different throats of Chang 7 sandstone.

Reservoir Type	Sample No	Movable fluid controlled by different throats								
		Large throat			Medium throat			Small throat		
		P_{t1} (%)	S_{mt1} (%)	Φ_{t1} (%)	P_{t2} (%)	S_{mt2} (%)	Φ_{t2} (%)	P_{t3} (%)	S_{mt3} (%)	Φ_{t3} (%)
I	2	63.59	36.23	2.86	23.32	13.28	1.05	13.09	7.45	0.59
	3	54.93	28.39	3.19	22.29	11.52	1.29	22.78	11.77	1.32
	4	54.10	29.71	2.97	21.83	11.98	1.20	24.07	13.22	1.32
	5	74.19	48.76	8.62	22.61	14.86	2.87	3.20	2.10	0.48
II	6	75.06	31.96	3.16	12.19	5.19	0.51	12.75	5.43	0.54
	7	64.41	23.47	1.08	9.55	3.48	0.28	26.04	9.49	2.46
	9	68.57	35.96	1.75	6.54	3.43	0.17	24.88	13.05	0.64
	10	40.64	10.31	1.69	31.97	8.11	1.33	27.39	6.95	1.39
	12	70.56	25.00	2.51	18.35	6.50	0.65	11.09	3.93	0.39
III	15	14.68	2.38	0.15	56.24	9.12	0.90	29.06	4.71	0.31
	16	24.67	2.68	0.41	53.66	5.83	0.90	21.67	2.35	0.36
	17	67.01	3.70	0.51	13.64	0.85	0.10	19.35	0.76	0.15
	19	24.72	3.06	0.27	21.89	2.71	0.24	53.39	6.61	0.59

Note: Sm_{t1}, Sm_{t2}, and S_{mt3} are movable fluid saturation controlled by the large throat, medium throat pores, and small throat, respectively. P_{t1}, P_{t2}, and P_{t3} are movable fluid proportions controlled by the large throat, medium throat pores, and small throat, respectively; Φ_{t1}, Φ_{t2}, and Φ_{t3} are movable fluid porosity controlled by the large throat, medium throat pores, and small throat, respectively.

Table 5
Pore structure parameters of Chang 7 tight sandstone samples.

Type	No	Depth (m)	Maximum pore-throat radius (μm)	Weighted average of pore-throat radius (μm)	Sorting coefficient	Maximum mercury Saturation (%)	Minimum residual mercury saturation (%)	Displacement pressure (Mpa)
I	1	1666.88	0.252	0.072	1.34	66.29	50.47	2.91
	4	1054.13	0.253	0.063	1.33	82.60	57.96	2.90
	5	1227.75	0.474	0.092	2.04	61.74	45.07	1.55
II	6	1669.16	0.099	0.024	3.164	65.42	45.79	7.39
	7	1436.2	0.473	0.110	2.46	59.04	44.08	1.55
	10	1428.45	0.100	0.021	2.38	57.11	38.69	7.39
	12	1437.2	0.073	0.018	3.05	42.47	27.83	10.07
	13	1607.06	0.054	0.013	2.34	45.10	25.96	13.73
III	15	1434.90	0.037	0.015	2.74	42.56	29.71	19.86
	16	1427.26	0.054	0.015	3.87	38.71	24.75	13.73
	17	1429.82	0.054	0.015	3.60	39.45	22.26	13.73
	19	1451.6	0.073	0.0189	3.94	28.20	19.25	10.07

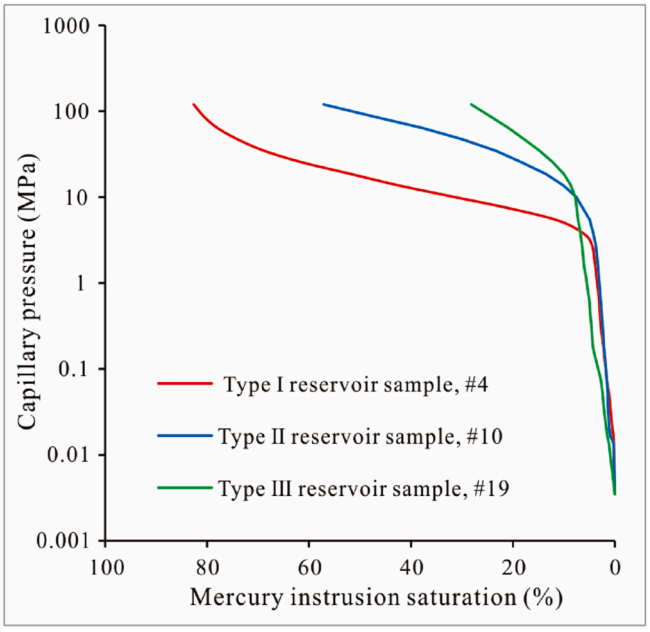

Fig. 7. Capillary pressure curves in the samples of the Chang 7 reservoir.

is lower, ranging from 6.23% to 23.21% (mean 14.52%).

The pore radius amplitude constructed from NMR data can reflect the volume of different pores and the fluid content in different pores. For example, in sample # 5, the movable fluid distribution in different pores can be obtained from the difference of pore radius amplitude constructed from NMR data under water-saturated conditions and after centrifugation at 417 psi (Fig. 6). The movable fluid parameters of samples are shown in Table 3. The movable fluids of Chang 7 sandstone are mainly distributed in nanopores and submicron pores, accounting for 9.05–90.14% (mean 51.30%) and 6.39–67.35% (mean 33.66), respectively. A small amount of movable fluid is distributed in micron pores, accounting for 0–46.95% (averaging 14.88%). The movable fluid content in different pores of three types of reservoirs is quite different. The movable fluid is mainly distributed in submicron pores for the type I reservoir, accounting for 27.27–67.35% (mean 52.24%), followed by nanopores and micron pores, accounting for 9.05–42.24% (averaging 27.63%) and 6.27–46.95% (mean 20.20%), respectively. For the type II reservoir, the movable fluids are mainly distributed in nanopores and submicron pores, accounting for 39.77–67.40% (mean 50.23%) and 20.52–51.90% (mean 33.51%), respectively. A few movable fluids are distributed in the micron pores. For the type III reservoir, the movable fluids are mainly distributed in nanopores, accounting for 58.25–90.14% (averaging 72.47%). There're fewer or almost no movable fluids in micron and submicron pores.

The fluidity of the fluid in pores is controlled by throat size (Li et al., 2018a, 2020a; Qiao et al., 2020a). The fluid controlled by the large throat has strong fluidity, while the small throat has weak fluidity. The movable fluid content controlled by different throats can be identified

Table 6
The content of minerals of Chang 7 tight sandstone samples.

Reservoir Type	Sample No	Mineral composition (wt.%)							Clay composition (wt.%)		
		Q	F	Ca	Clay	Pyrite	Anhydrite	Augite	I/S	I	Ch
I	1	36.30	23.80	8.00	26.69	0.80	3.00	1.41	16.01	2.81	7.87
	2	35.70	42.50	5.70	12.29	0.00	3.30	0.51	7.55	2.56	2.18
	3	30.40	40.50	4.00	25.10	0.00	0.00	0.00	10.79	4.27	10.04
	4	31.30	39.30	5.00	22.70	1.70	0.00	0.00	4.99	2.95	14.76
II	6	26.20	25.40	9.00	34.00	0.00	4.40	1.00	18.02	4.08	11.90
	7	26.80	25.80	7.20	37.3	0.00	2.90	0.00	19.77	3.73	13.80
	8	31.70	42.60	3.10	19.30	0.00	3.30	0.00	9.07	3.09	7.14
	9	27.0	35.20	19.60	18.20	0.00	0.00	0.00	7.28	3.64	7.28
	10	24.00	24.00	1.60	47.22	1.20	0.38	1.60	28.46	6.37	12.39
	11	23.10	14.80	7.50	42.00	8.20	2.60	1.80	17.18	3.66	21.15
	12	28.00	33.31	0.50	38.19	0.00	0.00	0.00	16.04	2.29	19.86
	13	29.90	32.10	3.80	34.20	0.00	0.00	0.00	20.52	7.87	5.81
III	14	24.00	31.10	0.00	44.90	0.00	0.00	0.00	19.31	6.74	18.86
	15	29.30	33.10	9.00	28.60	0.00	0.00	0.00	11.95	4.17	12.51
	16	19.10	18.60	2.40	52.18	1.70	1.92	4.10	36.55	7.89	7.75
	17	24.60	17.90	4.30	44.69	4.40	1.31	2.80	32.21	5.44	7.04

Q: Quartz; F: Feldspar; Ca: Carbonate; I/S: Illite/Smectite; I: Illite; Ch: Chlorite.

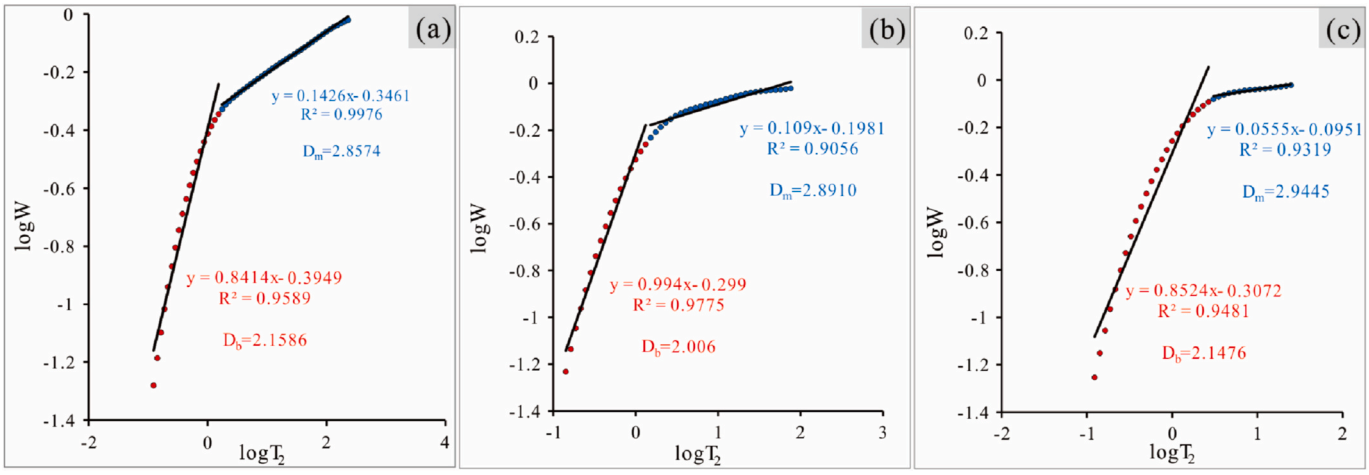

Fig. 8. Fractal dimension curve of representative samples of three types of reservoirs from NMR data. (a): No #1 of type I reservoir; (b): No #6 of type II reservoir; (c): No #13 of type III reservoir.

Table 7
Fractal dimensions of tight sandstone samples based on NMR data.

Reservoir Type	Sample No	$T_2>T_{2cutoff}$		$T_2<T_{2cutoff}$	
		Fractal dimension (D_m)	R^2	Fractal dimension (D_b)	R^2
I	1	2.8574	0.9976	2.1586	0.9589
	2	2.7318	0.9972	2.5387	0.9647
	3	2.8101	0.9056	2.1595	0.9823
	4	2.7596	0.9721	2.2591	0.9970
	5	2.7053	0.9870	2.2481	0.8987
II	6	2.891	0.9056	2.0060	0.9775
	7	2.9297	0.8619	2.0030	0.9769
	8	2.9267	0.8819	2.1865	0.9961
	9	2.8837	0.8643	2.2300	0.9811
	10	2.9249	0.9768	2.1966	0.9246
	11	2.8825	0.9885	2.0925	0.9448
	12	2.9153	0.9721	2.1359	0.9669
	13	2.9231	0.9641	2.1565	0.9419
III	14	2.9445	0.9319	2.1476	0.9481
	15	2.9856	0.9412	2.0375	0.9560
	16	2.9044	0.9799	2.1306	0.9503
	17	2.8987	0.9864	2.1404	0.9328
	18	2.9425	0.9490	2.1233	0.9522
	19	2.9291	0.9422	2.0972	0.8669

by loading different centrifugal forces on water-saturated cores. According to formula (1), when the centrifugal forces were 42 psi, 208 psi, and 417 psi, the corresponding throat diameters (D_t) were 0.5 μm, 0.1 μm, and 0.05 μm, respectively. According to the centrifugal experiment conditions, the throat can be divided into the large throat (D_t larger than 0.5 μm), medium throat (D_t of 0.1–0.5 μm), and small throat (D_t of 0.05–0.1 μm). For example, in sample #5, the movable fluid content controlled by different throats can be obtained by recording the movable fluid centrifuged out by different centrifugal forces (Fig. 6). Table 4 shows the movable fluid content controlled by different throats in samples. Different throats mainly control the movable fluids in different types of reservoirs. For the type I reservoir, the movable fluid content is mainly controlled by large throats, accounting for 54.10–74.19% (mean 61.70%), followed by medium throats, accounting for 21.83–23.32% (averaging 22.51%). For type II reservoir, the movable fluid is mainly controlled by a large throat, accounting for 40.64–75.06%, with a typical value of 63.85%, followed by a small throat, accounting for 11.09–27.39% (mean 20.43%). For the type III reservoir, the movable fluid is controlled by three types of the throat. The movable fluid controlled by the large, medium, and small throats accounted for 4.68–67.01% (mean 32.77%), 13.64–56.24% (mean 36.36%), and 19.35–53.39% (mean 30.87%), respectively.

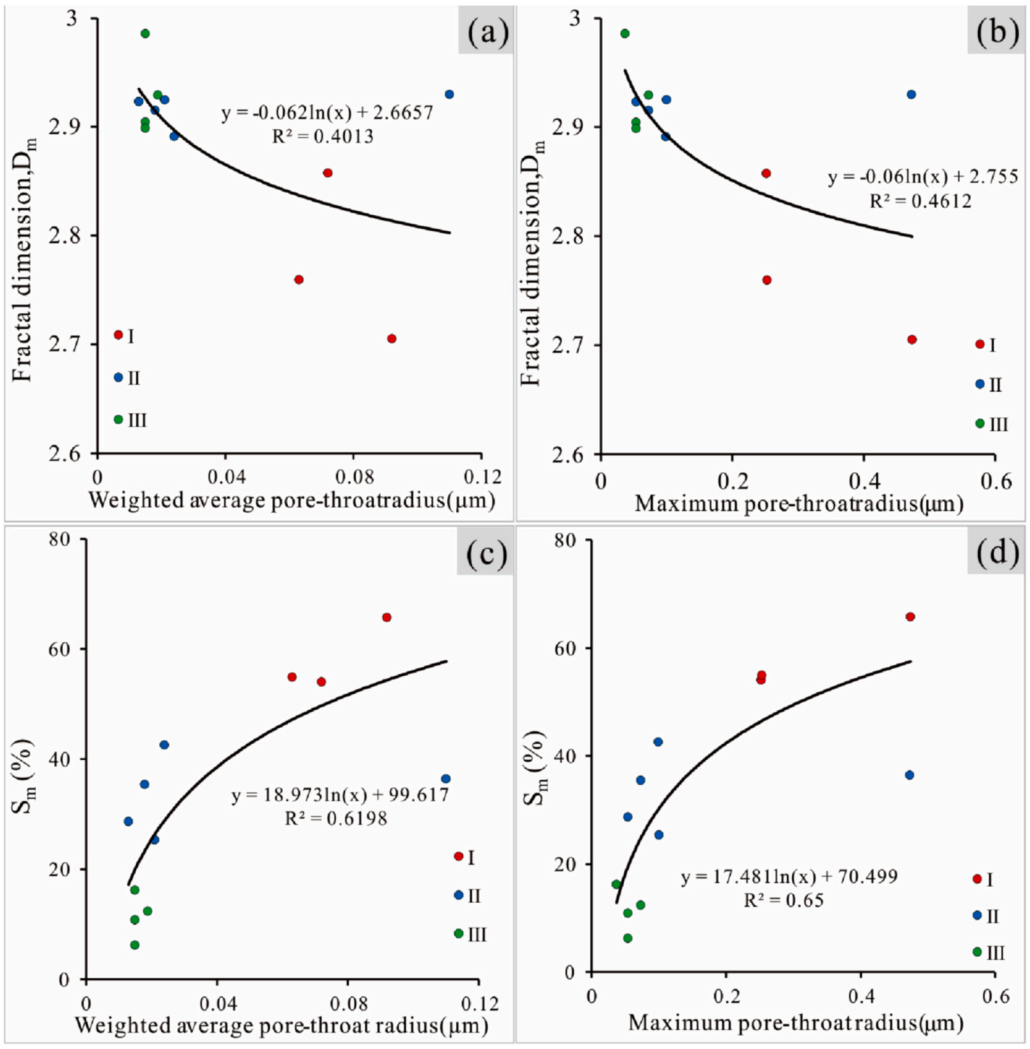

Fig. 9. Correlation of the weighted average pore-throat radius and maximum pore-throat radius with movable fluid saturation and fractal dimension. Movable fluid saturation vs. weighted average pore-throat radius (a) and maximum pore-throat radius (b); Fractal dimension vs. weighted average pore-throat radius (c) and maximum pore-throat radius (d).

4.4. Pore-throat structure parameters and mineral compositions

4.4.1. Pore-throat structure parameters

The characteristic parameters of the pore structure of Chang 7 tight sandstone samples can be obtained by HPMI (Table 5). The capillary pressure curve of the type I reservoir has deviated to the lower left of the figure (Fig. 7). It shows a relatively low displacement pressure (the point on the curve where the mercury initially enters the pore-throat system of the sample), ranging from 1.55 MPa to 2.91 MPa (mean 2.46 MPa). The sorting coefficient is 1.33–2.04 (averaging 1.57). The weighted average pore radius ranges from 0.062 μm to 0.091 μm, with a typical value of 0.075 μm, and the maximum mercury saturation is 61.74–82.60% (mean 70.21%). The average porosity is 10.05%, and the average permeability is 0.0982 × 10^{-3}μm^2. Therefore, type I reservoirs should have relatively higher storage and penetration capacity. The common pores in type I reservoirs are intergranular dissolution pores and intragranular dissolution pores, along with a small number of micro-fractures (Fig. 3a–c).

The capillary pressure curve of type II reservoirs has higher displacement pressure (Fig. 7). The average porosity is 4.79%, while the mean permeability is 0.0129 × 10^{-3}μm^2. The displacement pressure ranges from 1.55 MPa to 13.73 MPa, with a typical pressure of 8.37 MPa. The weighted average pore radius ranges from 0.014 μm to 0.11 μm (averaging 0.037 μm), and maximum mercury saturation is 42.47–65.41% (mean 53.83%), while the sorting coefficient is 2.34–3.16 (averaging 2.68). The relatively small pore throat and the high displacement pressure indicated the corresponding reservoir with relatively lower storage and percolation capacity. Intergranular dissolution pores and inter-crystalline pores are common in type II reservoirs, and there are a few intergranular dissolution pores (Fig. 3d–f).

The capillary pressure curve of type III reservoirs is featured by high displacement pressure (Fig. 7). The displacement pressure varies from 10.07 MPa to 19.86 MPa, with an average of 14.34 MPa. The average porosity is 4.90%, and the average permeability is 0.0064 × 10^{-3}μm^2. The maximum mercury saturation is distributed in the range of 28.20–42.56% (mean 37.23%). The sorting coefficient is relatively large, distributed in 2.74–3.94 (mean 3.54). Type III reservoirs are characterized by very fine pore throats and very high displacement pressure. Therefore, type III reservoir should have very low storage and percolation capacity. Type III reservoirs are dominantly inter-crystalline pores, with a few dissolution pores (Fig. 3 g-i).

4.4.2. Mineral compositions

The quantitative mineral composition in the Chang 7 tight sandstone reservoir samples is analyzed by XRD. The mineral compositions are listed in Table 6. The quartz content ranges from 19.10–36.30% (mean

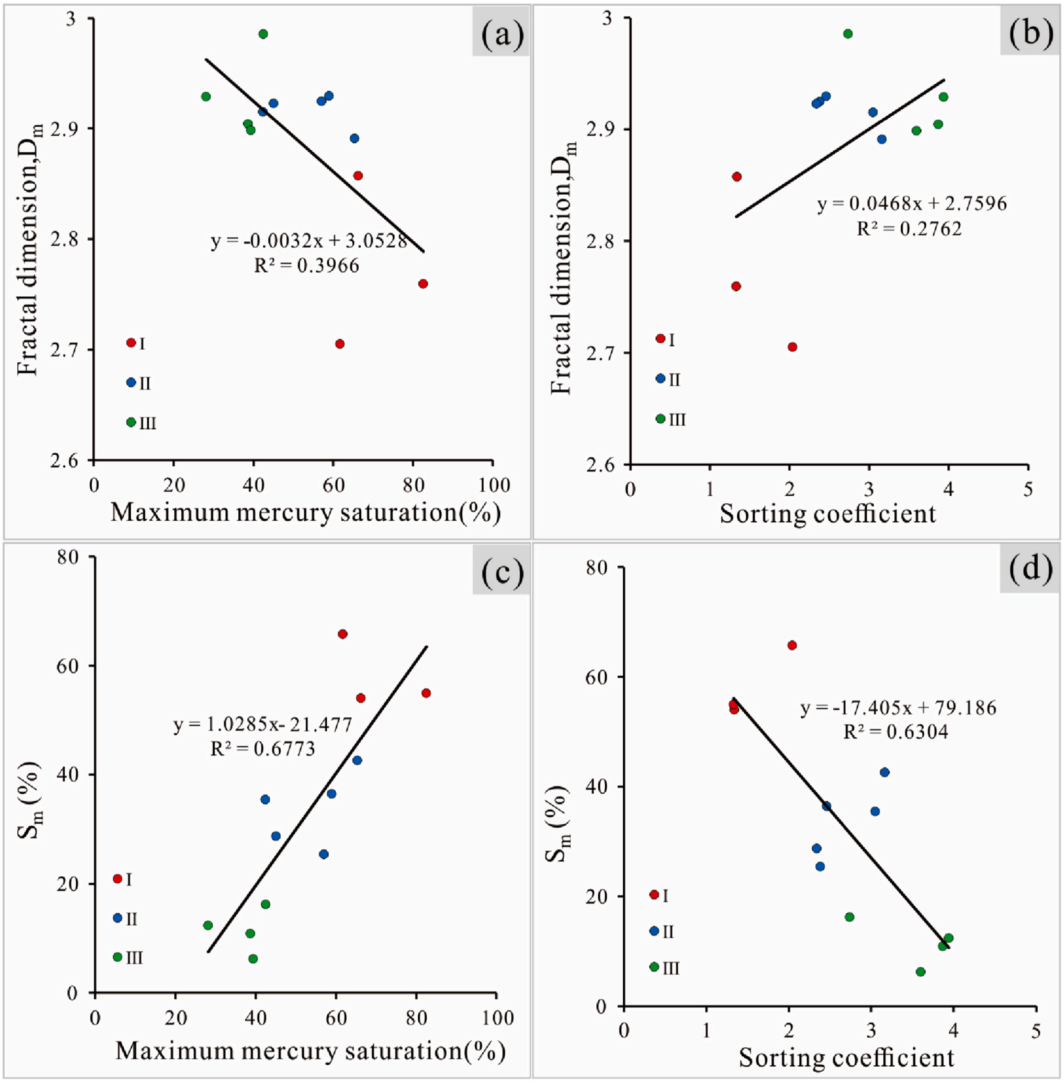

Fig. 10. Correlation of the maximum mercury saturation and sorting coefficient with fractal dimension and movable fluid saturation. Fractal dimension vs. maximum mercury saturation (a) and sorting coefficient (b); Movable fluid saturation vs. maximum mercury saturation (c) and sorting coefficient (d).

25.09%). The feldspar content mainly ranges from 14.80% to 42.60% (averaging 23.14%). The clay content is high, ranging from 12.80% to 57.90%, with a typical value of 32.98%. From type I reservoir to type III reservoir, the contents of quartz and feldspar tend to decrease, while clay mineral content tends to increase. The content of carbonate minerals is relatively low (mean 6.97%). The carbonate content of type I and II reservoirs is higher than type III reservoirs. The samples of Chang 7 sandstone also contain a minor amount of pyrite, anhydrite, and augite. The clay predominantly consists of the illite/smectite mixed layer, chlorite, and illite. The content of the illite/smectite mixed layer is the highest, accounting for 4.99–36.55% of total minerals (averaging 17.23%), followed by chlorite, accounting for 2.18–21.15% (mean 11.27%). From type I reservoir to type III reservoir, the content of mixed layer illite-smectite tends to increase. The illite content is the lowest, accounting for 2.81–7.89% (mean 4.47%). The mineral compositions of Chang 7 tight sandstone samples are quite different, indicating that the mineral compositions are complex and the compositional maturity is low.

4.5. Fractal theory and fractal dimensions based on NMR

Since Mandelbrot proposed the fractal concept, the fractal theory has been widely employed to investigate the micro-pore structure characteristics of porous media (Amadu and Pegg, 2018; Mandelbrot et al., 1984; Zhang and Andreas, 2014; Zhao et al., 2020). Fractal dimension can quantitatively reflect the irregularity and complexity of pore structure, which can be calculated by gas adsorption, mercury injection capillary pressure, and NMR techniques (Amadu and Pegg, 2018; Li et al., 2020b; Liu et al., 2018; Zhang et al., 2021). The calculation model of fractal dimension based on NMR experiment data has been discussed in detail in previous studies (Fan et al., 2019; Mandelbrot et al., 1984; Zhou et al., 2016), which can be expressed in the following formula.

$$W = \left(\frac{T_2}{T_{2\,max}}\right)^{3-D} \tag{10}$$

where: W is the accumulative pore volume fraction; T_2 is the transverse relaxation time; T_{2max} is the maximum value of T_2; D is the fractal dimension.

Taking the logarithm of both sides of Eq. (10), the calculation formula of fractal dimension can be changed as follows:

$$log\,(W) = (3-D)\,log\,(T_2) + (D-3)\,log\,(T_{2\,max}) \tag{11}$$

According to the NMR experimental data, the straight-line slope (k) between log W and logT_2 can be obtained, and the fractal dimension can be calculated from Eq. (12).

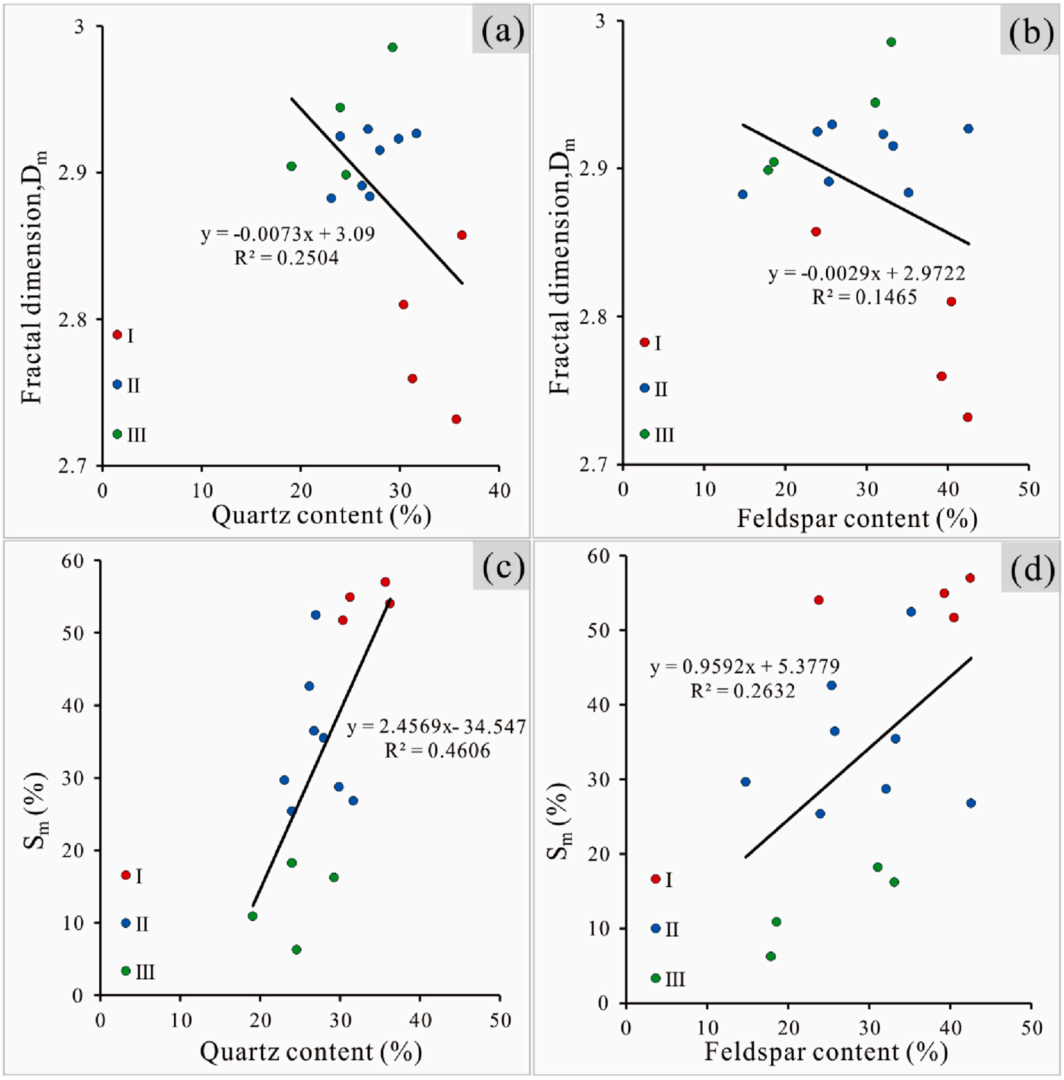

Fig. 11. The scattered plots of quartz and feldspar vs. the fractal dimension and movable fluid saturation. Fractal dimension vs. quartz (a) and feldspar (b); Movable fluid saturation vs. quartz (c) and feldspar (d).

$$3 - D = k \tag{12}$$

Log (W)–log (T_2) plot is constructed to present the fractal characteristics of different types of reservoirs (Fig. 8). According to the occurrence characteristics of fluids (movable fluids and bound fluids), the curve of log(W) versus log (T_2) can be divided into two segments at the positions of log ($T_{2cutoff}$). Both have a correlation coefficient of greater than 0.85, indicating that Chang 7 tight sandstone samples have two sections of the fractal structure and can be characterized by fractal geometry theory (Fig. 8). The fractal dimension D_m ($T_2 > T_{2cutoff}$) and D_b ($T_2 < T_{2cutoff}$) and corresponding correlation coefficients are shown in Table 7. D_m is related to larger pores (movable fluid pores), and D_b is related to small pores (bound fluid pores). The D_m and D_b are between 2.0 and 3.0, implying that fractal theory can apply to movable fluid and bound fluid pores in the study area. Since the focus of this study is the occurrence characteristics of the movable fluid, only the fractal dimension D_m ($T_2 > T_{2cutoff}$) are used for subsequent analysis. Table 7 shows the linear fitting curves' correlation coefficient (R^2) is distributed in the range of 0.8643–0.9976 (mean 0.9414), showing a good correlation. The fractal dimension (D_m) of Chang 7 sandstone mainly ranges from 2.7053 to 2.9856 (mean 2.8814), indicating that movable fluid pores of Chang 7 reservoir are characterized by strong heterogeneity. As shown in Table 7, the D_m varies with the reservoir types. The D_m of type I reservoir is relatively small, ranging from 2.7053 to 2.8574 (mean 2.7728). The D_m of the type II reservoir is distributed between 2.8837 and 2.9727 (averaging 2.9096). The D_m of type III reservoir is relatively large, ranging from 2.8987 to 2.9856 (mean 2.9340). The above-mentioned results indicate that the heterogeneity of type II and III reservoirs is stronger than type I reservoirs.

5. Discussion

NMR curves are classified according to the characteristics of the T_2 spectrum and petrophysical parameters as described in the previous sections. Therefore, the following part discusses the effects of pore structure, mineral composition, and pore size distribution on fractal dimension and movable fluid saturation instead of considering physical properties.

5.1. Relationship between pore structure parameters vs. fractal dimension and movable fluid saturation

Due to the limited number of samples, the relationship among pore structure parameters, fractal characteristics, and movable fluid content in different reservoirs is not feasible, and the results are uncertain. Therefore, the relationship among pore structure parameters, fractal

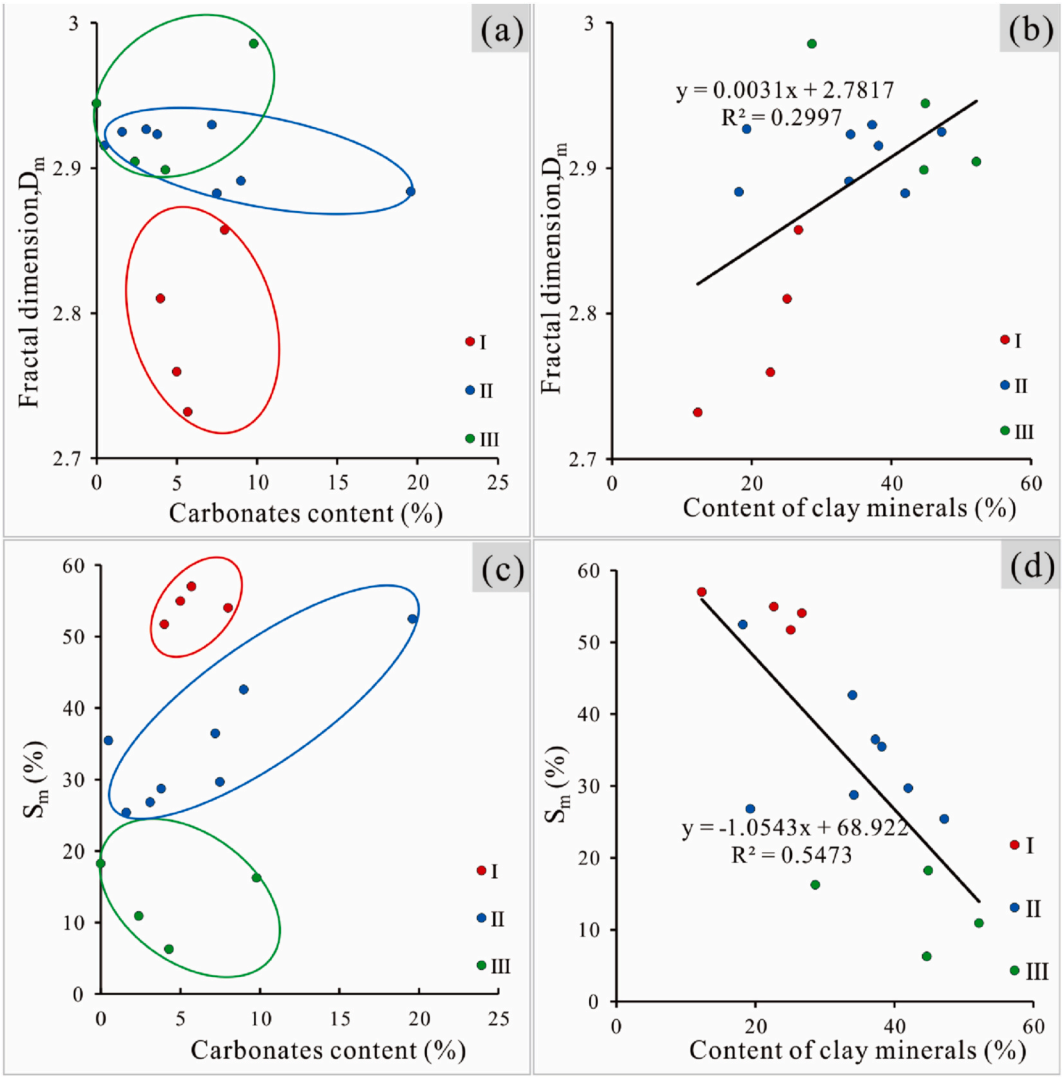

Fig. 12. The relationship between carbonates and clay minerals vs. the fractal dimension and movable fluid saturation. Fractal dimension vs. carbonates (a) and clay minerals (b); Movable fluid saturation vs. carbonates (c) and clay minerals (d).

dimensions, and movable fluid parameters is not classified. Generally, the larger the weighted average pore throat radius, the larger the pore throat. Fig. 9 displays that the tight sandstone reservoir with more large pore throats often corresponds to weak heterogeneity and higher movable fluid content. It is similar to the previous research on the relationship between pore-throat size and fractal dimension and movable fluid content in tight sandstone reservoirs (Li et al., 2019a; Schmitt Rahner et al., 2018; Wang et al., 2019). The larger weighted average pore-throat radius and maximum pore-throat radius correspond to a relatively gentle fitted curve, indicating the heterogeneity and movable fluid content are more sensitive to the smaller pore-throat radius.

The maximum mercury saturation could reflect the pore-throat volume (Lai et al., 2018b). Generally, larger pore-throat volume corresponds to more effective large pore throats (Qu et al., 2020). The maximum mercury saturation shows a weak negative correlation with fractal dimension (Fig. 10a), while it shows a positive association with movable fluid saturation (Fig. 10c). The type I reservoir with larger maximum mercury saturation means more effective large pore throats, weak heterogeneity, and better connectivity, which lead to high movable fluid content and is beneficial to the hydrocarbon accumulation. However, type III reservoir with smaller maximum mercury saturation has more small pore throats, strong heterogeneity, and bad connectivity, resulting in low movable fluid content. The sorting coefficient reflects the uniformity degree of the pore-throat size distribution (Lai et al., 2018b). Small sorting coefficient means uniform reservoir. Fig. 10b and d shows the reservoir with a smaller sorting coefficient generally corresponds to even pore-throat size distribution and weak heterogeneity, which is beneficial to higher movable fluid content.

5.2. *Effect of mineral compositions on fractal dimension and movable fluid saturation*

The brittle mineral framework is highly susceptible to overburden pressure, which is conducive to the preservation of residual intergranular pores. In contrast, the ductile clastic minerals are susceptible to compaction, which are not conducive to the preservation of residual intergranular pores (Ajdukiewicz and Larese, 2012; Fan et al., 2019; Qiao et al., 2020b; Qu et al., 2020; Yang et al., 2020). The relationship of various minerals with fractal dimension and movable fluid saturation is presented in Figs. 11 and 12. It can be seen from Fig. 11a and b that high content quartz and feldspar weaken the heterogeneity and are conducive to the connectivity to a certain extent. The positive relationships between the movable fluid saturation and the contents of quartz and feldspar confirm that quartz and feldspar can provide favorable conditions developing connected pores in tight sandstone (Fig. 11c and d).

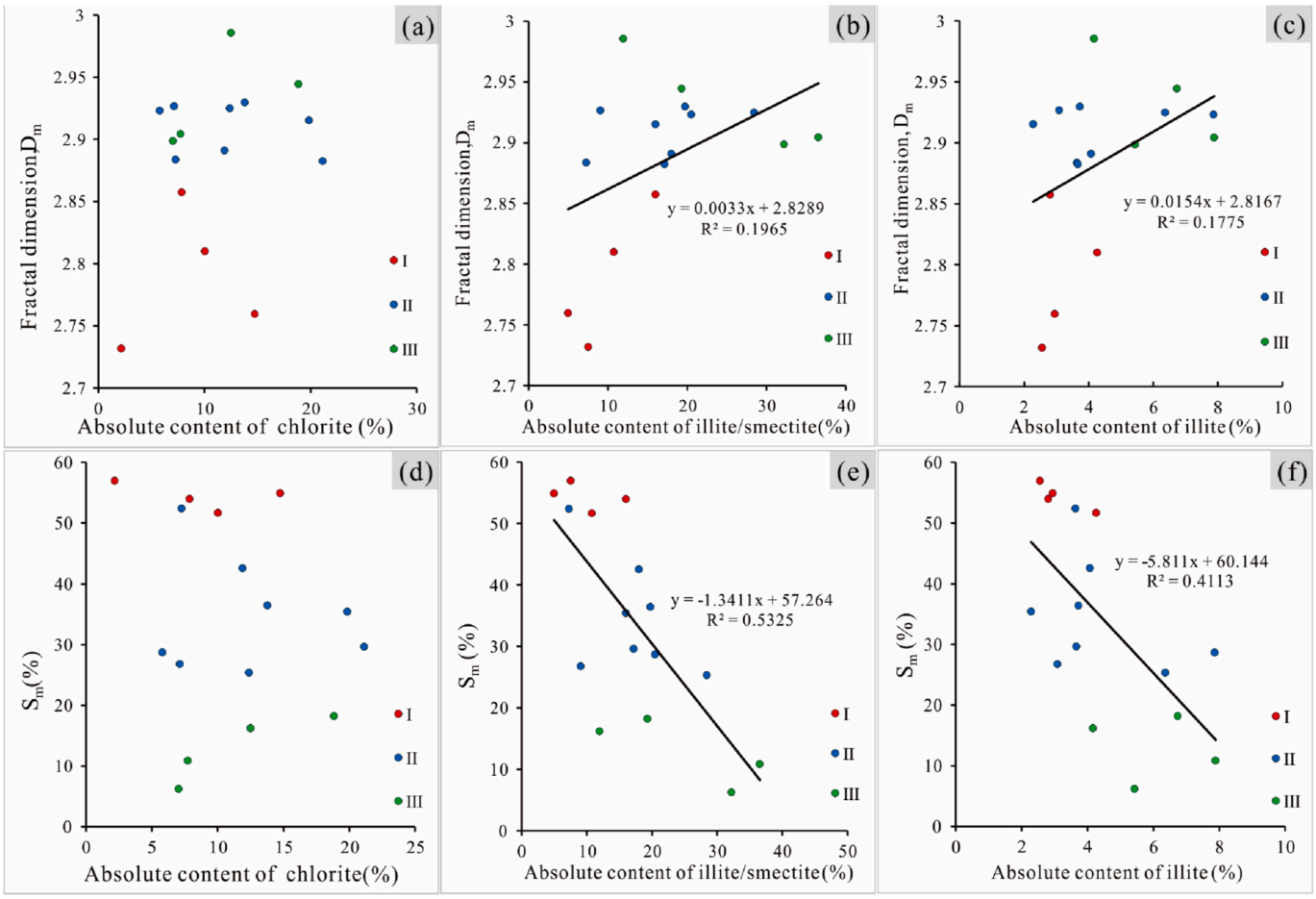

Fig. 13. Correlation of the absolute content of clay minerals with fractal dimension movable fluid saturation. Fractal dimension vs. the absolute content of chlorite (a), illite/smectite (b), and illite (c); Movable fluid saturation vs. the absolute content of chlorite (d), illite/smectite (e), and illite (f).

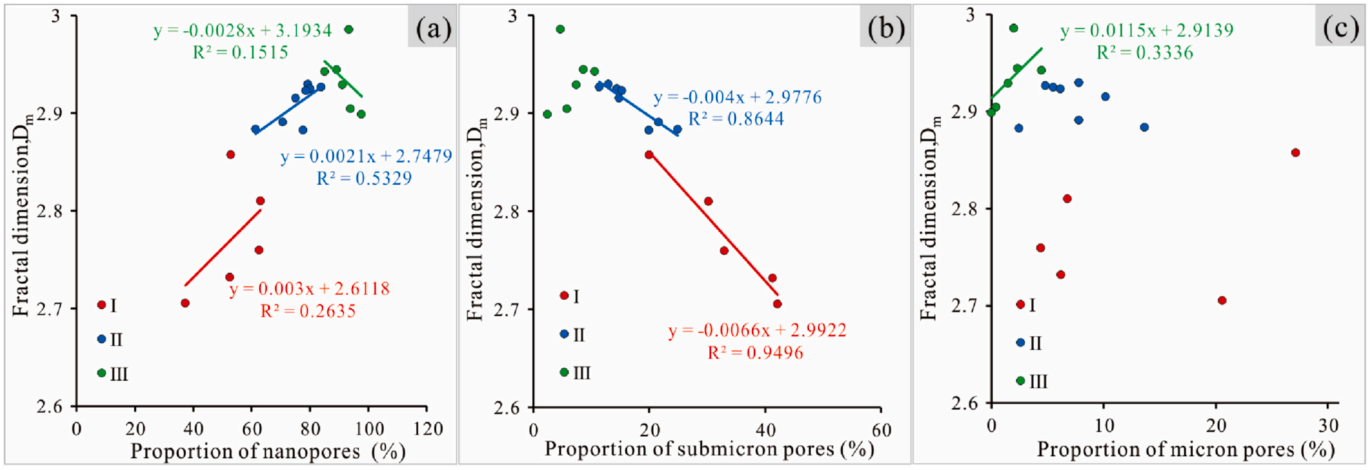

Fig. 14. The correlation of the fractal dimension with various pores. (a). Nanopores proportion, (b). Submicron pores proportion, (c). And micron pores proportion.

The movable fluid saturation decreases with the increase of quartz in some samples because the authigenic quartz crystal in the pore enhances the heterogeneity and weakens the connectivity, hindering the fluid flow in the pore. Similarly, the movable fluid saturation in some samples decreases with the increase of feldspar content. It might be due to feldspar dissolution, which produces dissolution pores and provides a source for the precipitation of clay minerals (Qiao et al., 2020b; Zhang et al., 2020).

The effect of carbonate cement on pore connectivity varies with the formation period of carbonate (Qiao et al., 2020b; Yang et al., 2020). Carbonate cementation after dissolution can destroy the reservoir pore structure and decreases pore connectivity. However, the dissolution of early carbonate cement may improve pore connectivity. The relationship between carbonate content and fractal dimension is different in the three types of reservoirs (Fig. 12a, c). For type I and II reservoirs, the relationships among carbonate content, D_m, and S_m may be related to

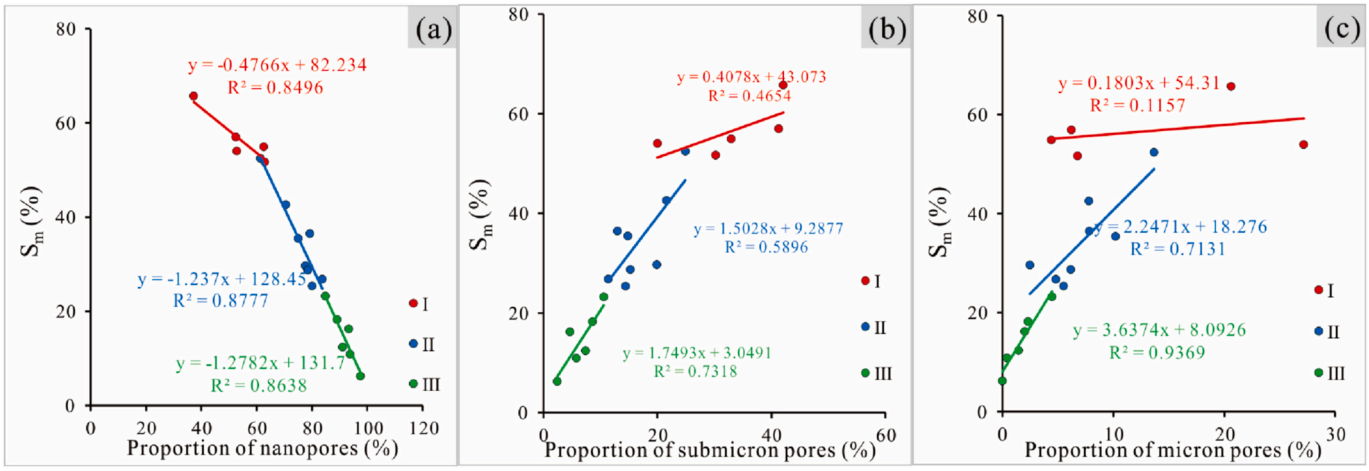

Fig. 15. The correlation of movable fluid saturation with various pores. (a). Nanopores proportion, (b). Submicron pores proportion, (c). And micron pores proportion.

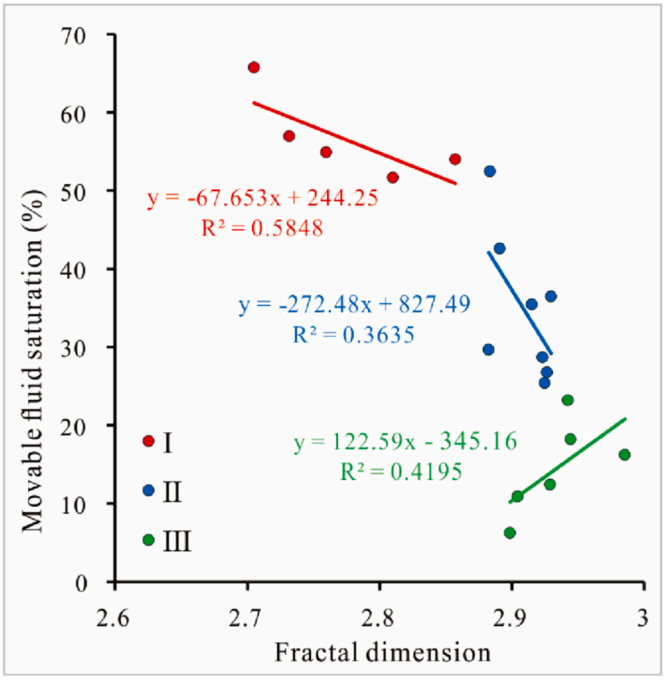

Fig. 16. The relationship between movable fluid saturation and fractal dimension.

the carbonate cementation after dissolution (Fig. 12a, c). However, for the type III reservoir, carbonate content is negatively correlated with D_m and positively correlated with S_m, which may be due to the dissolution of carbonate minerals formed in the early stage (Fig. 12a, c). It can be seen from Fig. 12b and d that the development of clay mineral blocks the pore system. It deteriorates the connectivity of pores, enhances heterogeneity, and further inhibits the enrichment of movable fluid. The S_m of some samples increases with the increase of clay minerals content. It may be because the clay minerals can resist compaction to a certain degree, conducive to pore preservation (Qiao et al., 2020b). It also shows that the influence of clay minerals on movable fluid content has a dual character.

The influence of clay minerals on D_m and S_m is due to the joint action of different types of clay minerals. The influence of clay minerals on the heterogeneity has been noticed, and the movable fluid content varies with clay types (Fig. 13). As shown in Fig. 13, the relationships among different types of clay minerals, D_m, and S_m indicate that the influence of clay minerals on fractal characteristics and movable fluid content is mainly reflected in the illite/smectite mixed layer and illite. The chlorite in the intergranular pore can complicate the pore structure and hinder the connectivity of pores (Ajdukiewicz and Larese, 2012; Fan et al., 2019; Yang et al., 2020). However, the chlorite wrapped on the particle surface can enhance the anti-compaction ability and inhibit the overgrowth of quartz, which is conducive to preserving pores and improving the connectivity of pores (Ajdukiewicz and Larese, 2012; Qiao et al., 2020b). Therefore, the influence of chlorite on the fractal characteristics and movable fluid content is uncertain, showing the dual character of chlorite.

5.3. *Effect of pore size distribution on fractal dimension and movable fluid saturation*

It can be inferred from Fig. 14 that the relationship between D_m and pore size distribution parameters varies with reservoir types. For the type I and II reservoirs, the D_m is positively related to submicron pores (Fig. 14b) while negatively correlated with nanopores (Fig. 14a). These results indicate that tight sandstone reservoirs with a higher submicron pore concentration exhibit weaker heterogeneity, whereas the higher proportion of nanopores corresponds to stronger heterogeneity. Fig. 14c indicates the micron pore has no detectable effect on the heterogeneity of type I and II reservoirs due to fewer micron pores. Additionally, it can be seen from Fig. 14a and c that type III reservoirs with more nanopores generally correspond to weaker heterogeneity, while more micron pores usually correspond to stronger heterogeneity of pore structure. It may be because the storage space of type III reservoir is mainly composed of nanopores, and the pore size distribution has limited influence on the heterogeneity of type III reservoir.

The reservoir's storage capacity varies with the distribution of pore size (Cao et al., 2016; Gao and Li, 2016; Zhang et al., 2019). Reservoirs with more large pores generally have stronger storage capacity, while reservoirs with more small pores have weaker storage capacity (Cao et al., 2016; Lai et al., 2018a, 2018b; Qiao et al., 2020a). Fig. 15 shows the development of submicron and micron pores is conducive to the fluid flow and contributes to the higher movable fluid content, while the nanopores have the opposite effect. The correlation between movable fluid saturation and pore size distribution parameters varies with reservoir types. For the type II and III reservoirs, the connectivity of micron pores is better than submicron pores. Moreover, micron pores are more beneficial to fluid enrichment and flow than submicron pores, making the movable fluid saturation slightly more sensitive to micron pores than submicron pores (Fig. 15b and c). For the type I reservoir, the

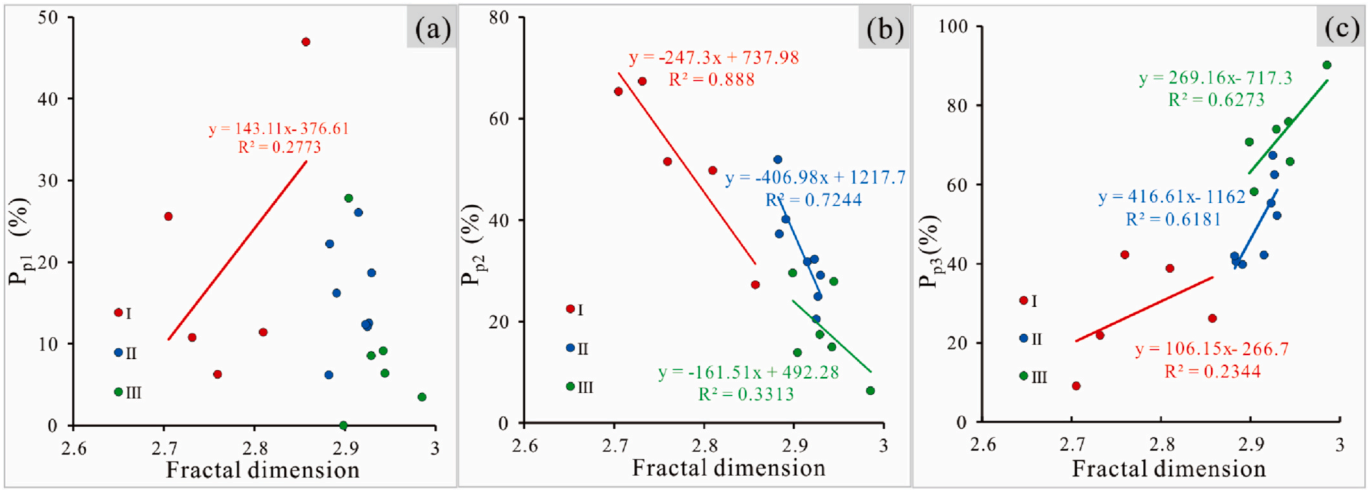

Fig. 17. The relationship between fractal dimension vs. movable fluid proportion in micron pores (P_{p1}) (a), submicron pores (P_{p2}) (b), and in nanopores (P_{p3}) (c).

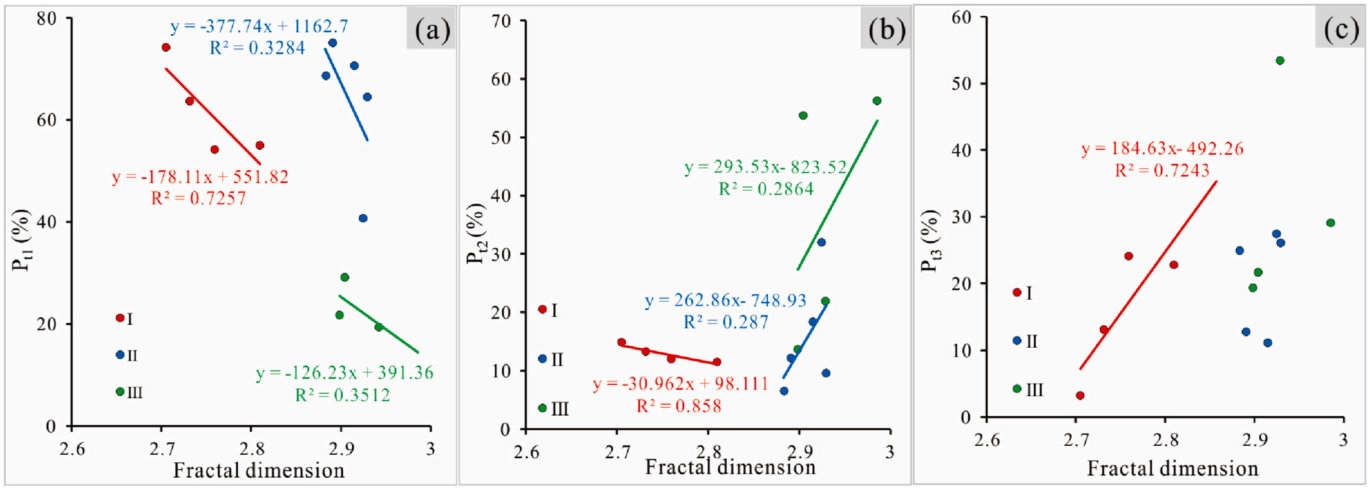

Fig. 18. The relationship between fractal dimension and movable fluid proportion is controlled by the large throat (P_{t1}) (a), medium throat (P_{t2}) (b), and small throat (P_{t3}) (c).

S_m is slightly more sensitive to submicron pores than micron pores. In addition, the S_m of type I reservoir is closely related to nanopores and submicron pores while weakly related to micron pores. It may be because there are micron pores in type I reservoirs. Most of them are disconnected pores or surrounded by smaller throats.

5.4. *Effect of heterogeneity on the movable fluid distribution*

Fig. 16 shows the scattered plots of the fractal dimension versus movable fluid saturation. In the type I and II reservoirs, the D_m has negative correlations with the S_m, indicating that the strong heterogeneity reduces the movable fluid content in type I and II reservoirs. It may be because the storage space of type III reservoir is mainly contributed by nanopores, resulting in a positive correlation between D_m and S_m.

Fig. 17 shows that heterogeneity has various effects on the occurrence characteristics of the movable fluid in different reservoirs. A certain number of movable fluids are distributed in the micron pores of type I reservoir, deciphering a weak correlation between the P_{p1} and D_m (Fig. 17a). The P_{p1} of type II and III reservoirs has no obvious correlation with D_m (Fig. 17a), which may be due to the weak influence of micron pores on the heterogeneity of type II and III reservoirs and very few movable fluids in micron pores. It can be inferred from Fig. 17b that the heterogeneity strongly influences the movable fluid content in submicron pores of type I and II reservoirs. It may be because most of the movable fluids of type I and II reservoirs are distributed in submicron pores. Type I and II reservoirs with more submicron pores correspond to weaker heterogeneity and better connectivity, resulting in higher movable fluid content. Submicron pores have no obvious influence on the heterogeneity of type III reservoir and fewer movable fluid in submicron pores, resulting in a weak correlation between P_{p2} and D_m (Fig. 17b). Fig. 17c indicates that the reservoir with strong heterogeneity corresponds to a high movable fluid proportion in the nanopores. The influence of nanopores on the heterogeneity of type I reservoir is weaker. The movable fluid content in nanopores is relatively lower, resulting in a poor association between the P_{p3} and D_m (Fig. 17c). Overall, the influence of heterogeneity on the movable fluid in type I reservoirs is mainly reflected in submicron pores. In contrast, the movable fluid of type II reservoirs is mainly reflected in nanopores and submicron pores. However, the movable fluid of type III reservoir is mainly reflected in nanopores.

Fig. 18 shows the heterogeneity has various influences on controlling the effect of different throats in the three types of reservoirs. The movable fluid controlled by the large throat is mainly distributed in submicron and micron pores, resulting in a negative correlation between D_m and P_{t1} (Fig. 18 a). The movable fluid controlled by small and medium throats is mainly distributed in pores of different scales, resulting

in the relationship between D_m and P_{t2} and P_{t3} varies with reservoir types (Fig. 18b and c). For the type I reservoir, D_m is negatively correlated with the P_{t2}, which may be because these movable fluids are mainly distributed in submicron and micron pores (Fig. 18b). However, the D_m is positively correlated with the P_{t3} because these movable fluids are mainly distributed in nanopores (Fig. 18c). For the type II and III reservoirs, the D_m has a weak positive correlation with the P_{t2}, while it has no significant correlation with the P_{t3} (Fig. 18b). It is because these movable fluids are mainly distributed in nanopores and submicron pores that have opposite effects on heterogeneity. Generally, for the type I reservoir, strong heterogeneity weakens the effect of the large and medium throat and improves the effect of small throats. For the type II and III reservoirs, strong heterogeneity inhibits the effect of the large throat and enhances the effect of medium throats, while it has no obvious effect on the effect of the small throat.

6. Conclusions

(1) The Chang 7 sandstone in the Ansai area is a typical tight sandstone with low porosity and ultra-low permeability. Various pores have been observed in the tight sandstone of Chang 7 Member, including i. intergranular dissolution pores, ii. intragranular dissolution pores, iii. residual intergranular pores, iv. inter-crystalline pores, v. microfractures. Quartz, feldspar, and clays are the main mineral constituents, and the clay predominantly consists of an illite/smectite mixed layer, chlorite, and illite.

(2) The Chang 7 reservoir has been divided into three types (type I, II, and III) based on the distribution of the T_2 spectrum and petrophysical parameters. These reservoirs are characterized by different movable fluid distributions, diverse pore size distributions, various fractal structures, and distinct pore structures. The characteristic of Type I reservoir are relatively weak heterogeneity, well connectivity, higher movable fluid content, and it is mainly composed of nanopores and submicron pores. In contrast, type II and III reservoirs are characterized by strong heterogeneity, poor connectivity, and low movable fluid content and are chiefly comprised of nanopores. Movable fluids in type I and III reservoirs are mainly distributed in submicron pores and nanopores, respectively. The type II reservoir is chiefly distributed in both two kinds of pores, i.e., submicron pores and nanopores. The large throats mainly control the moveable fluid content in type I and II reservoirs, whereas, in type III reservoirs, it is chiefly controlled by all three types of throats, i.e., large, medium, and small throats.

(3) In this research, several possible factors are analyzed which can affect the fractal features and movable fluid content of the reservoir, including pore structure, pore size distribution, mineral compositions. Reservoirs with more submicron pores often correspond to weak heterogeneity and high movable fluid content. Fractal dimension exhibits poor correlation with pore structure parameters and mineral compositions. The movable fluid saturation is significantly affected by pore structures and weakly by mineral compositions. The influence of heterogeneity on movable fluid varies with reservoir types. The heterogeneity influence on movable fluids in type I, II, and III reservoirs is mainly reflected in submicron pores, submicron-nanopores, and nanopores, respectively. The strong heterogeneity weakens the effect of large and medium throats in the type I reservoirs, while it improves the effect of small throats. The strong heterogeneity inhibits the effect of large throats and enhances the effect of medium throats in type II and III reservoirs, while it has no obvious control on the effect of small throats.

Declaration of competing interest

The authors declare that they have no known competing financial interests or personal relationships that could have appeared to influence the work reported in this paper.

Acknowledgments

This research is financially funded by the National Natural Science Foundation of China with grant number 41872127. The authors thank the No.1 Oil Production Plant, PetroChina Changqing Oilfield Company, for providing a database. Additionally, the authors are thankful to anonymous reviewers for reviewing this paper and their valuable comments and suggestions, which significantly improved the quality of this research.

References

Ajdukiewicz, J.M., Larese, R.E., 2012. How clay grain coats inhibit quartz cement and preserve porosity in deeply buried sandstones: observations and experiments. AAPG (Am. Assoc. Pet. Geol.) Bull. 96 (11), 2091–2119.
Al-Mahrooqi, S.H., Grattoni, C.A., Muggeridge, A.H., Zimmerman, R.W., Jing, X.D., 2006. Pore-scale modelling of NMR relaxation for the characterization of wettability. J. Petrol. Sci. Eng. 52 (1–4), 172–186.
Amadu, M., Pegg, M.J., 2018. Theoretical and experimental determination of the fractal dimension and pore size distribution index of a porous sample using spontaneous imbibition dynamics theory. J. Petrol. Sci. Eng. 167, 785–795.
Awan, R.S., et al., 2021. Organic geochemical evaluation of Cretaceous Talhar shale for shale oil and gas potential from lower Indus basin, Pakistan. J. Petrol. Sci. Eng. 200, 108404.
Cao, Z., et al., 2016. Pore structure characterization of Chang-7 tight sandstone using MICP combined with N2GA techniques and its geological control factors. Sci. Rep. 6 (1), 36919.
Chen, M., et al., 2018. Contributions of pore-throat size distribution to reservoir quality and fluid distribution from NMR and MIP in tight sandy conglomerate reservoirs. Arabian J. Geosci. 12 (9).
Clarkson, C.R., et al., 2012a. Characterization of tight gas reservoir pore structure using USANS/SANS and gas adsorption analysis. Fuel 95, 371–385.
Clarkson, C.R., Jensen, J.L., Pedersen, P.K., Freeman, M., 2012b. Innovative methods for flow-unit and pore-structure analyses in a tight siltstone and shale gas reservoir. AAPG (Am. Assoc. Pet. Geol.) Bull. 96 (2), 355–374.
Cui, J., Zhu, R., Luo, Z., Li, S., 2019. Sedimentary and geochemical characteristics of the Triassic Chang 7 member shale in the Southeastern Ordos Basin, Central China. Petrol. Sci. 16 (2), 285–297.
Dai, C., et al., 2019. Oil migration in nanometer to micrometer sized pores of tight oil sandstone during dynamic surfactant imbibition with online NMR. Fuel 245, 544–553.
Daigle, H., Johnson, A., 2015. Combining mercury intrusion and nuclear magnetic resonance measurements using percolation theory. Transport Porous Media 111 (3), 669–679.
Deng, Z.S., Ma, Y.T., Feng, Z.H., 2014. Note: a novel piezoelectrically driven pipette using centrifugal force. Rev. Sci. Instrum. 85 (5), 056106.
Desbois, G., Urai, J.L., Kukla, P.A., Konstanty, J., Baerle, C., 2011. High-resolution 3D fabric and porosity model in a tight gas sandstone reservoir:A new approach to investigate microstructures from mm- to nm-scale combining argon beam cross-sectioning and SEM imaging. J. Petrol. Sci. Eng. 78 (2), 243–257.
Elton, N.J., Salt, P.D., 1996. Particle statistics in quantitative X-ray diffractometry. Powder Diffr. 11 (3), 218–229.
Eslami, M., Kadkhodaie-Ilkhchi, A., Sharghi, Y., Golsanami, N., 2013. Construction of synthetic capillary pressure curves from the joint use of NMR log data and conventional well logs. J. Petrol. Sci. Eng. 111, 50–58.
Fan, X., et al., 2019. Pore structure evaluation of tight reservoirs in the mixed siliciclastic-carbonate sediments using fractal analysis of NMR experiments and logs. Mar. Petrol. Geol. 109, 484–493.
Fu, J., Li, S., Xu, L., Niu, X., 2018. Paleo-sedimentary environmental restoration and its significance of Chang 7 member of Triassic Yanchang Formation in Ordos Basin, NW China. Petrol. Explor. Dev. 45 (6), 988–1008.
Gao, H., Li, H., 2015. Determination of movable fluid percentage and movable fluid porosity in ultra-low permeability sandstone using nuclear magnetic resonance (NMR) technique. J. Petrol. Sci. Eng. 133, 258–267.
Gao, H., Li, H., 2016. Pore structure characterization, permeability evaluation and enhanced gas recovery techniques of tight gas sandstones. J. Nat. Gas Sci. Eng. 28, 536–547.
Ge, X., Fan, Y., Zhu, X., Chen, Y., Li, R., 2015. Determination of nuclear magnetic resonance T2 cutoff value based on multifractal theory — an application in sandstone with complex pore structure. Geophysics 80 (1), D11–D21.
Guo, R., et al., 2020. Fractal characteristics of pore-throat structure and permeability estimation of tight sandstone reservoirs: a case study of Chang 7 of the Upper Triassic Yanchang Formation in Longdong area, Ordos Basin, China. J. Petrol. Sci. Eng. 184, 106555.

Hossain, Z., Grattoni, C.A., Solymar, M., Fabricius, I.L., 2011. Petrophysical properties of greensand as predicted from NMR measurements. Petrol. Geosci. 17 (2), 111–125.
Huang, H., et al., 2020. A method to probe the pore-throat structure of tight reservoirs based on low-field NMR: insights from a cylindrical pore model. Mar. Petrol. Geol. 117, 104344.
Jia, C., Zhang, M., Zhang, Y., 2012. Unconventional hydrocarbon resources in China and the prospect of exploration and development. Petrol. Explor. Dev. 39 (2), 1137–1149.
Jorand, R., Fehr, A., Koch, A., Clauser, C., 2011. Study of the variation of thermal conductivity with water saturation using nuclear magnetic resonance. J. Geophys. Res. 116 (B8), B08208.
Lai, J., et al., 2018a. Investigation of pore structure and petrophysical property in tight sandstones. Mar. Petrol. Geol. 91, 179–189.
Lai, J., Wang, G., Ran, Y., Zhou, Z., Cui, Y., 2016. Impact of diagenesis on the reservoir quality of tight oil sandstones: the case of Upper Triassic Yanchang Formation Chang 7 oil layers in Ordos Basin, China. J. Petrol. Sci. Eng. 145, 54–65.
Lai, J., et al., 2018b. A review on pore structure characterization in tight sandstones. Earth Sci. Rev. 177, 436–457.
Lai, J., et al., 2019. Pore structure and fractal characteristics of Ordovician Majiagou carbonate reservoirs in Ordos Basin, China. AAPG (Am. Assoc. Pet. Geol.) Bull. 103 (11), 2573–2596.
Li, P., et al., 2019a. The characteristics of movable fluid in the Triassic lacustrine tight oil reservoir: a case study of the Chang 7 member of Xin'anbian Block, Ordos Basin, China. Mar. Petrol. Geol. 102, 126–137.
Li, P., Sun, W., Wu, B., Gao, Y., Du, K., 2018a. Occurrence characteristics and influential factors of movable fluids in pores with different structures of Chang 63 reservoir, Huaqing Oilfield, Ordos Basin, China. Mar. Petrol. Geol. 97, 480–492.
Li, P., et al., 2018b. Occurrence characteristics and main controlling factors of movable fluids in Chang 81 reservoir, Maling Oilfield, Ordos Basin, China. J. Pet. Explor. Prod. Technol. 9 (1), 17–29.
Li, T., et al., 2020a. Reservoir characteristics and evaluation of fluid mobility in organic-rich mixed siliciclastic-carbonate sediments: a case study of the lacustrine Qiketai Formation in Shengbei Sag, Turpan-Hami Basin, Northwest China. J. Petrol. Sci. Eng. 185, 106667.
Li, X., et al., 2019b. Fractal characterization of nanopore structure in shale, tight sandstone and mudstone from the Ordos Basin of China using nitrogen adsorption. Energies 12 (4), 583.
Li, Z., Liu, D., Cai, Y., Wang, Y., Si, G., 2020b. Evaluation of coal petrophysics incorporating fractal characteristics by mercury intrusion porosimetry and low-field NMR. Fuel 263, 116802.
Liu, M., et al., 2018. Determining the segmentation point for calculating the fractal dimension from mercury injection capillary pressure curves in tight sandstone. J. Geophys. Eng. 15 (4), 1350–1362.
Liu, S., Yang, S., 2000. Upper Triassic – jurassic sequence stratigraphy and its structural controls in the western Ordos Basin, China. Basin Res. 12, 1–18.
Liu, Z., et al., 2020. Application of nuclear magnetic resonance (NMR) in coalbed methane and shale reservoirs: a review. Int. J. Coal Geol. 218, 103261.
Machabeli, G., Rogava, A., 1994. Centrifugal force: a gedanken experiment. Phys. Rev. 50 (1), 98.
Mandelbrot, B.B., Passoja, D.E., Paullay, D.E., 1984. Fractal character of fracture surfaces in porous media. Nature 308, 721–722.
Mao, G., Lai, F., Li, Z., Wei, H., Zhou, A., 2020. Characteristics of pore structure of tight gas reservoir and its influence on fluid distribution during fracturing. J. Petrol. Sci. Eng. 193, 107360.
Mao, Z., He, Y., Ren, X., 2005. An improved method of using NMR T2 distribution to evaluate pore size distribution. Chin. J. Geophys. 48 (2), 412–418.
Mozley, P.S., Heath, J.E., Dewers, T.A., Bauer, S.J., 2016. Origin and heterogeneity of pore sizes in the mount simon sandstone and Eau Claire formation: implications for multiphase fluid flow. Geosphere 12 (4), 1341–1361.
Oluwadebi, A.G., Taylor, K.G., Ma, L., 2019. A case study on 3D characterisation of pore structure in a tight sandstone gas reservoir: the Collyhurst Sandstone, East Irish Sea Basin, northern England. J. Nat. Gas Sci. Eng. 68, 102917.
Pope, C.G., 1997. X-ray diffraction and the Bragg equation. J. Chem. Educ. 74 (1), 129.
Qiao, J., et al., 2020a. Insights into the pore structure and implications for fluid flow capacity of tight gas sandstone: a case study in the upper paleozoic of the Ordos Basin. Mar. Petrol. Geol. 118, 104439.
Qiao, J., et al., 2020b. Effects of mineralogy on pore structure and fluid flow capacity of deeply buried sandstone reservoirs with a case study in the Junggar Basin. J. Petrol. Sci. Eng. 189, 106986.
Qin, Y., et al., 2021. Pore structure and connectivity of tight sandstone reservoirs in petroleum basins: a review and application of new methodologies to the Late Triassic Ordos Basin, China. Mar. Petrol. Geol. 129, 105084.
Qu, Y., et al., 2020. Pore–throat structure and fractal characteristics of tight sandstones in Yanchang Formation, Ordos Basin. Mar. Petrol. Geol. 120, 104573.
Rezaee, R., Saeedi, A., Clennell, B., 2012. Tight gas sands permeability estimation from mercury injection capillary pressure and nuclear magnetic resonance data. J. Petrol. Sci. Eng. 88–89, 92–99.
Rosenbrand, E., Fabricius, I.L., Fisher, Q., Grattoni, C., 2015. Permeability in Rotliegend gas sandstones to gas and brine as predicted from NMR, mercury injection and image analysis. Mar. Petrol. Geol. 64, 189–202.
Schmitt, M., Halisch, M., Müller, C., Fernandes, C.P., 2016. Classification and quantification of pore shapes in sandstone reservoir rocks with 3-D X-ray micro-computed tomography. Solid Earth 7 (1), 285–300.
Schmitt Rahner, M., Halisch, M., Peres Fernandes, C., Weller, A., Sampaio Santiago dos Santos, V., 2018. Fractal dimensions of pore spaces in unconventional reservoir rocks using X-ray nano- and micro-computed tomography. J. Nat. Gas Sci. Eng. 55, 298–311.
Shabaninejad, M., Middlelton, J., Fogden, A., 2018. Systematic pore-scale study of low salinity recovery from Berea sandstone analyzed by micro-CT. J. Petrol. Sci. Eng. 163, 283–294.
Testamanti, M.N., Rezaee, R., 2017. Determination of NMR T2 cut-off for clay bound water in shales: a case study of Carynginia Formation, Perth Basin, Western Australia. J. Petrol. Sci. Eng. 149, 497–503.
Timur, A., 1969. Pulsed nuclear magnetic resonance studies of porosity, movable fluid, and permeability of sandstones. J. Petrol. Technol. 6, 775–786.
Tinni, A., Odusina, E., Sulucarnain, I., Sondergeld, C., Rai, C.S., 2015. Nuclear-magnetic-resonance response of brine, oil, and methane in organic-rich shales. SPE Reservoir Eval. Eng. 18 (3), 400–406.
Tong, X., et al., 2018. Distribution and potential of global oil and gas resources. Petrol. Explor. Dev. 45 (4), 727–736.
Wang, B., Zhao, X., Zhou, W., Chang, B., Xu, H., 2020a. Quantitative characterization of pore connectivity and movable fluid distribution of tight sandstones: a case study of the upper Triassic Chang 7 member, Yanchang Formation in Ordos Basin, China. Geofluids 2020, 1–13.
Wang, F., Zeng, F., 2020. Novel insights into the movable fluid distribution in tight sandstones using nuclear magnetic resonance and rate-controlled porosimetry. Nat. Resour. Res. 29 (5), 3351–3361.
Wang, J., Cao, Y., Liu, K., Gao, Y., Qin, Z., 2019. Fractal characteristics of the pore structures of fine-grained, mixed sedimentary rocks from the Jimsar Sag, Junggar Basin: implications for lacustrine tight oil accumulations. J. Petrol. Sci. Eng. 182, 106363.
Wang, W., et al., 2020b. Qualitative and quantitative characterization of multiple factors that influence movable fluid saturation in lacustrine deep-water gravity-flow tight sandstones from the Yanchang Formation, southern Ordos Basin, China. Mar. Petrol. Geol. 121, 104625.
Wu, J., et al., 2021. Fractal characteristics of pore networks and sealing capacity of Ordovician carbonate cap rocks: a case study based on outcrop analogues from the Tarim Basin, China. AAPG (Am. Assoc. Pet. Geol.) Bull. 105 (2), 437–479.
Washburn, E., 1921. The dynamics of capillary flow. Phys. Rev. 17 (3), 273–283.
Wu, Y., et al., 2019. A comprehensive study on geometric, topological and fractal characterizations of pore systems in low-permeability reservoirs based on SEM, MICP, NMR, and X-ray CT experiments. Mar. Petrol. Geol. 103, 12–28.
Xu, H., et al., 2019. Characterization of pore throat size distribution in tight sandstones with nuclear magnetic resonance and high-pressure mercury intrusion. Energies 12 (8), 1528.
Xu, Y., Liu, L., Zhu, Y., 2021. Characteristics of movable fluids in tight sandstone reservoir and its influencing factors: a case study of Chang 7 reservoir in the Southwestern of Ordos Basin. J. Pet. Explor. Prod. Technol. 11 (9), 3493–3507.
Yan, J., et al., 2020. Sensitive parameters of NMR T2 spectrum and their application to pore structure characterization and evaluation in logging profile: a case study from Chang 7 in the Yanchang Formation, Heshui area, Ordos Basin, NW China. Mar. Petrol. Geol. 111, 230–239.
Yang, H., et al., 2016. Exploration potential of shale oil in Chang7 member, upper Triassic Yanchang Formation, Ordos Basin, NW China. Petrol. Explor. Dev. 43 (4), 560–569.
Yang, L., Wang, S., Jiang, Q., You, Y., Gao, J., 2020. Effects of microstructure and rock mineralogy on movable fluid saturation in tight reservoirs. Energy Fuels 34 (11), 14515–14526.
Yang, Y., Li, W., Ma, L., 2005. Tectonic and stratigraphic controls of hydrocarbon systems in the Ordos basin A multicycle cratonic basin in central China. AAPG (Am. Assoc. Pet. Geol.) Bull. 89, 255–269.
Yao, Y., Liu, D., 2012. Comparison of low-field NMR and mercury intrusion porosimetry in characterizing pore size distributions of coals. Fuel 95, 152–158.
Yuan, X., et al., 2015. Lacustrine fine-grained sedimentary features and organicrich shale distribution pattern: a case study of Chang 7 Member of Triassic Yanchang Formation in Ordos Basin, NW China. Petrol. Explor. Dev. 42 (1), 37–47.
Zang, Q., et al., 2021a. Occurrence models of movable fluid in lacustrine sandstone reservoir of Chang 7 member in the Heshui block, Ordos Basin, China. J. Earth Sci.
Zang, Q., et al., 2021b. Comparison of Pore Size Distribution, Heterogeneity and Occurrence Characteristics of Movable Fluids of Tight Oil Reservoirs Formed in Different Sedimentary Environments: a Case Study of Chang 7 Member of Ordos Basin, China. Natural Resources Research.
Zhang, F., et al., 2019. A multiscale comprehensive study on pore structure of tight sandstone reservoir realized by nuclear magnetic resonance, high pressure mercury injection and constant-rate mercury injection penetration test. Mar. Petrol. Geol. 109, 208–222.
Zhang, M., et al., 2021. Fluid distribution and pore structure multifractal characteristics analysis of coal measure mudstone. J. Nat. Gas Sci. Eng. 88, 103810.
Zhang, P., Lee, Y.I., Zhang, J., 2020. Diagenetic controls on the reservoir quality of tight oil-bearing sandstones in the upper Triassic Yanchang Formation, Ordos Basin, North-Central China. J. Petrol. Geol. 43 (2), 225–244.
Zhang, Z., Andreas, W., 2014. Fractal dimension of pore-space geometry of an Eocene sandstone formation. Geophysics 79 (6), D377–D387.
Zhao, H., et al., 2020. Micro-pore multifractal characteristics of Benxi formation sandstone reservoir in Gaoqiao area, Ordos Basin. Bullet. Geol. Sci. Technol. 39 (6), 175–184.
Zhao, P., Wang, Z., Sun, Z., Cai, J., Wang, L., 2017. Investigation on the pore structure and multifractal characteristics of tight oil reservoirs using NMR measurements: Permian Lucaogou Formation in Jimusaer Sag, Junggar Basin. Mar. Petrol. Geol. 86, 1067–1081.

Zhao, Y., et al., 2021. Multifractal analysis of coal pore structure based on NMR experiment: a new method for predicting T2 cutoff value. Fuel 283, 119338.
Zhou, S., Liu, D., Cai, Y., Yao, Y., 2016. Fractal characterization of pore–fracture in low-rank coals using a low-field NMR relaxation method. Fuel 181, 218–226.
Zhou, T., et al., 2019. Multi-scale quantitative characterization of pore distribution networks in tight sandstone by integrating FE-SEM, HPMI, and NMR with the constrained least squares algorithm. Energies 12 (18), 3514.
Zou, C., et al., 2012. Tight gas sandstone reservoirs in China: characteristics and recognition criteria. J. Petrol. Sci. Eng. 88–89, 82–91.